



UNIVERSITÀ DEGLI STUDI DI “ROMATRE”

DOTTORATO DI RICERCA IN INGEGNERIA MECCANICA ED
INDUSTRIALE

CICLO XXV

Aeroacoustic, acoustic and fluid dynamic characterization of rectangular partial enclosures

Ph.D. Thesis

Tiziano Pagliaroli

Tutor:

Prof. Roberto Camussi

Coordinatore:

Prof. Edoardo Bemporad

Thesis submitted in partial fulfillment of the requirements for the degree of
Doctor of Philosophy Rome, Italy, April 2013

*a Eleonora,
per avermi accompagnato con amore*

*Like a vortex "what goes around, comes around"
(Anonimo)*

Acknowledgements

Primo fra tutti ringrazio il Prof. Roberto Camussi per l'occasione data. Un sincero ringraziamento va anche al gruppo di fluidodinamica dell' Università degli studi di RomaTre.

Tiziano

Contents

1	Background	16
1.1	Acoustic model	16
1.1.1	Introduction	16
1.1.2	Lumped model	18
1.2	Proper Orthogonal Decomposition	21
1.2.1	The Karhunen-Loeve Decomposition	23
1.2.2	Method of Snapshots	24
1.2.3	POD limit method: time coefficients information and interlink with the statistical behaviour of the fluid field	25
2	Experimental set-up	28
2.1	The experimental test case	28
2.2	Test Case	33
2.3	Air supply, collector, muffler	33
2.4	Particle Image Velocimetry	38
2.5	Wall pressure measurements	38
2.6	Modal Test	39
2.6.1	Aeroacoustic measurements	42
3	A single-vortex model for POD assessment	43
3.1	Aim	43
3.2	Introduction	43
3.3	Rankine vortex	44
3.4	The vortex perturbations analysis	47
3.5	Single vortex POD analysis	52

4	Results	55
4.1	Introduction	55
4.2	Fluid dynamic characterization	55
4.2.1	POD analysis	58
4.3	Acoustic numerical simulation	63
4.3.1	End-correction	68
4.4	Wall pressure fluctuation statistics	73
4.5	Concluding Remarks	84
A	Appendix	87
A.1	Particle Image Velocimetry	87
A.1.1	25 years of Particle Image Velocimetry	87
A.1.2	Introduction	88
A.1.3	Cross-correlation of images	89
A.1.4	Peak detection and subpixel interpolation	91
A.2	Acoustic simulation	91
A.2.1	Introduction to finite element methods	91
A.2.2	Boundary conditions	93
A.3	Introduction to Labview	95
A.4	Implemented softwares	97
A.4.1	SYNCHRO	97
A.4.2	easyPOD	97
	Bibliografy	102

List of Figures

1	Picture of trapped vortex combustor based on RPE geometry realized by Italian National Agency for New Technologies, Energy and Sustainable Economic Development (ENEA courtesy).	14
2	An example of power spectrum of the pressure fluctuation radiated from the combustor in reactive condition.	14
1.1	Schematic diagram of the RPE considered in quasi-monodimensional model.	18
1.2	Acoustic classification of the RPEs: representative equations, constrain conditions and sketch of the geometries.	22
1.3	Solutions of Eqs. 1.17 (<i>cubical HR</i> —), 1.16 (<i>long cavity HR</i> · —) and 1.13 (<i>double duct</i> — — —) yield with Newton's method. . .	23
2.1	RPE forward wall project (a) and a picture of the component realized (b).	29
2.2	Three part of hand-make multi-whole injector (a), multi-whole injector installed on RPE (b) , some commercial injectors installed on RPE (c) and some commercial connectors used to make RPE air supply (d).	30
2.3	Three part of the pipes mounted on RPE (a), side wall of RPE (b), forward and backward wall of the RPE where the injection system is fitted (c) a prototype of the RPE produced (d).	31
2.4	Picture of the RPE installed in the laboratory.	32
2.5	Picture of the RPE installed in the anechoic chamber.	32

2.6	Sketch of front view and transversal section of the rectangular partial enclosure test case, reporting the main symbols using in the text.	34
2.7	A conceptual design of a collector.	34
2.8	Picture of a couple of prototypes of collector.	35
2.9	Picture of a couple of prototypes of collector.	35
2.10	Picture of the last prototypes of muffler-collector.	36
2.11	Power spectrum of the noise emitted by collector empty (red dashed line) and filled with foam (black line).	36
2.12	Single-line diagram of the feedline system.	37
2.13	Conceptual design of the muffler-collector.	37
2.14	Three dimensional render of the PIV experimental set-up (a). Sketch of the three different FOV investigated.	39
2.15	Sketch of static pressure taps realized on the top wall of the RPE.	40
2.16	A conceptual render of the modal test.	41
2.17	Sketch of modal test set-up.	41
2.18	Sketch aeroacoustic experimental set-up.	42
3.1	The cylindrical coordinate system adopted for the description of the Rankine vortex model. The unit normal vectors set $(\mathbf{i}, \mathbf{j}, \mathbf{k})$ is reported in the point identified by coordinates (r, θ, z)	45
3.2	The Rankine vortex model is characterized by a flow that is always and everywhere parallel to the \mathbf{j} unit vector, so the only non null vector component is v_θ which is also the total velocity vector modulus. Note that at the characteristic length δ , the flow is continuous, but the flow regime changes from a solid rotation to a hyperbolic decrease for increasing distances.	47
3.3	Instantaneous pictures of velocity realizations for $\omega t = -\pi$, $\omega t = 0$ and $\omega t = \pi$ (from left to right). The Rankine vortex dynamic is provided by superimposing WTD on f_θ (figures a, b, c) and perturbing the vortex core position with the disturbance \hat{r} (figures d, e, f).	51

3.4	Fluctuating energy spectrum of the first four modes extracted by POD (a); Proper orthogonal decomposition modes identified by decomposition of the Rankine vortex dynamic simulation: mode 0, 1, 2, 3, 4, respectively corresponding to mean field (a), vortex asymmetric flapping (b), isotropic flapping, wandering, bouncing.	53
4.1	Sketch of the flow physics.	56
4.2	Averaged velocity field measured at $Re = 50271$ for different values of cavity aspect ratio: $\Gamma = 2.6$ (a), $\Gamma = 3.8$ (b). Azimuthal (\circ) and radial (Δ) velocity profiles extracted from the PIV data at $y = 73mm$ for $\Gamma = 2.6$ (c) and at $y = 90mm$ for $\Gamma = 3.8$ (d)	57
4.3	Pressure coefficient distribution along the top wall of the RPE.	58
4.4	Streamlines of the averaged velocity field, corresponding to FOV_2 and measured at $Re = 50271$ for $\Gamma = 2.6$ (a), $\Gamma = 3.8$ (b).	59
4.5	POD domain, evidenced by red and blue rectangle centered on the vortex core of the main scale formed in the cavity.	60
4.6	First four modes: 0 (a), 1(b), 2(c), 3(d), 4 (e) and eigenvalue spectrum obtained performing POD on Ω_1 domain (f).	61
4.7	Sketch of the dominant dynamic identified: vortex flapping (a) and vortex wandering (b).	62
4.8	First two modes: mode 1(a) and mode 2(b) provided computing POD on Ω_2 domain.	63
4.9	Average velocity (black solid line) and limit cases (red dashed line) profiles referred to the first mode(a). Average velocity (black solid line) and limit cases (red dashed line) profiles referred to the second mode (b). Average velocity (black solid line) and limit cases (red dashed line) iso-velocity line referred to the first mode(c). Average velocity (black solid line) and limit cases (red dashed line) iso-velocity line referred to the second mode(d).	64
4.10	First two modes for different Γ	65

4.11 Eigenvalue spectrum varying Γ	66
4.12 Sketch of the mesh realized.	67
4.13 First three modes occurring in the square RPE. Grey levels represent the SPL in an arbitrary scale.	69
4.14 First three modes occurring in the rectangular RPE: (a) first mode, (b) second longitudinal mode, (c) second transversal mode and (d) third mode. Grey levels represent the SPL in an arbitrary scale.	70
4.15 Frequency Response Function for the three different configu- rations: $\Gamma = 3.8$ (—), $\Gamma = 3.2$ (— — —), $\Gamma = 2.6$ (· · · · ·). . .	71
4.16 Enlargement of the exterior acoustic field simulated at the first mode frequency. The length of the exterior end correction δ_e is qualitatively estimated and superimposed on the figure. The grey levels represent the sound pressure level in arbitrary scale. . .	71
4.17 Frequency Response Function for three different configura- tions: $\Gamma = 3.8$ (—), $\Gamma = 3.2$ (— — —) and, $\Gamma = 2.6$ (· · · · ·). .	72
4.18 First mode frequency referred to $d = 50mm$ (\circ), $d = 40mm$ (\blacksquare), $d = 30mm$ (\diamond).	73
4.19 First mode experimental frequency versus frequency predict applying empirical-end correction. Linear fitting of the data is superimposed.	74
4.20 Power spectral density referred to microphone 5 obtained vary- ing Γ and keeping Re constant(a). First mode frequency, pro- vided by means aeroacoustic test (\triangle), superimposed to solu- tions of Eq. 1.17 (<i>cubical HR</i> —), Eq. 1.16 (<i>long cavity HR</i> —) and Eq. 1.13 (<i>double duct</i> — — —)(b).	75
4.21 Power spectral density of the wall pressure referred to station 1, the pressure is normalized by q_{in}^2 . The data are taken at $Re =$ 50271 and $\Gamma = 2.0, 2.6, 3.2, 3.8$ (a). The data are computed at $Re = 50271, 36865, 30163$ and $\Gamma = 3.8$ (b).	76

4.22	Normalized power spectral density referred to microphone 1 for $Re=50271$ (—), $Re=36865$ (---) and $Re=30163$ (· -) and $\Gamma = 2.6$ (a) and $\Gamma = 3.68$ (b). Normalized power spectral densities referred to microphone 5 computed for different Γ , $Re=50271$ (c). Normalized PSD computed at $Re=50271$ and different cavity aspect ratio: $\Gamma = 3.8$ (—), $\Gamma = 3.2$ (- - -) and $\Gamma = 2.6$ (· -) (d) . Averaged vorticity field (contour) and streamlines (white lines) obtained at $Re=50271$ for two values of cavity aspect ratio: $\Gamma = 2.6$ (e) and $\Gamma = 3.8$ (f).	78
4.23	Magnitude (- - -) and phase (—) of the cross-spectrum referred to microphones 1 and 2 computed for the square cavity at $Re = 50271$	80
4.24	Cross-correlation between microphone 1 and 2 computed after filtering the raw signal with low-pass filter (a) and high-pass filter (b). The curves are provided for three different Re numbers: 50271 (—), 36865 (· -) and 30163 (· · ·).	80
4.25	Cp_{rms} referred to all microphones computed for $Re=50271$ and different Γ : $\Gamma = 3.8$ (\square), $\Gamma = 3.2$ (\circ) and $\Gamma = 2.6$ (\triangle). . .	82
4.26	PDF of the wall pressure fluctuations reported in reduced variables. Different kind of markers correspond to different microphones: microphone 1 (\circ), microphone 2 (\square), microphone 3 (\triangle) and microphone 4 (\diamond); PDFs in (a) are computed at $\Gamma = 2.6$, PDFs in (b) are computed at $\Gamma = 3.8$ and compared with normal distribution (—).	83
4.27	Spectrum of the eigenvalues referred to $\Gamma = 2.6$ (\square) and $\Gamma = 3.8$ (\triangle).	83
4.28	First mode of the proper orthogonal decomposition obtained varying Γ from 3.8 (a) to 2.6 (c) (left to right).	84
A.1	Sketch of the scattering behaviour upon particles size.	88
A.2	Sketch of the PIV experimental set-up.	89
A.3	Mie scattering image of a rolled-up reactive jet.	89

A.4	Sketch of the domain where the acoustic response has been modeled.	94
A.5	Sketch of the wave propagation into a free-field outside a open-duct.	95
A.6	GUI of the Flowmeter (a), Laser (b) and Microphones (c). . .	98
A.7	Scheme of wiring of two different flow meter in a linear network.	99
A.8	Icon of easyPOD.	100
A.9	GUI of easyPOD.	100

List of Tables

2.1	Values of the test case geometrical parameters.	33
4.1	First three mode frequencies varying Γ	68
4.2	The convention velocities and convection-inlet velocity ratios for square and rectangular cavities and different Re numbers. .	81

Abstract

Wall pressure fluctuations generated by interaction of turbulent jets with the wall of rectangular partial enclosures (RPEs) are studied experimentally over a broad range of parameters. The scope of the present work is to characterize the propagation of the pressure perturbations in the RPEs by means of wall pressure auto-spectra, cross-spectra and cross-correlations measured through microphones located along the wall. In order to interpret the pressure measurement, the acoustic and fluid dynamic behaviours are investigated analytically, numerically and experimentally for several cavity-neck section ratios. The flow structures as the vortex formed in the cavity and the recirculation zone in the neck are studied in details. The acoustic behaviour of this geometry is investigated with particular emphasis on the first dominant mode analysis. It is pointed out that the first mode frequency scales as an Helmholtz resonator frequency. Taking into account this scaling a reduced form of the Strouhal number, that leads the spectra to collapse, is proposed. Furthermore it is found that the mechanism characterizing the pressure propagation at high frequency close to the bottom wall is strongly affected by the adverse pressure gradient that modifies the jet-wall interaction. The fluid dynamic contribution of the pressure fluctuations at high frequency is accompanied by a relevant acoustic effect characterized by a convection velocity close to the speed of sound at low frequency. The dynamic of the recirculation zone, characterized using the Proper Orthogonal Decomposition technique, plays an important role from the aeroacoustic viewpoint that produces in some conditions an increase of the wall pressure fluctuations at low frequency.

Introduction

Rectangular partial enclosures (RPEs), also named rectangular covered cavities, rectangular mufflers or rectangular expansion chambers are encountered in many industrial applications. For these reasons they have been extensively investigated from an analytical, experimental and numerical, viewpoint in the past. They are often used to suppress aerodynamic noise, e.g. in heating, ventilation and air conditioning. Different inlet-outlet configurations of RPE have been realized: offset or centered inlet-outlet, reverse flow, end-in and side-out [see Venkatesham et al., 2009]. Several observations have suggested that the pressure oscillations induced by aerodynamic noise into RPEs, generally fall into two categories, depending on whether the incoming jet flow is free or bounded on one side [see Keller, 1984, Keller and Escudier, 1983]. The latter category, most frequently appearing in practice [see Keller, 1982], is the object of the present investigation. These oscillations are a nuisance not only for the noise produced, but also for the possibility of inducing mechanical failures in pipe systems [see Ziada, 2010]. The aeroacoustic pulsations, generated by the coupling of flow instabilities with acoustic standing waves occurring in the geometry, are called *self-sustained* or *self-excited oscillations*. Typically this phenomenon was investigated in T-joint, safety valves and pipes with side branches, where a shear layer has been identified as the main sound source of aeroacoustic pulsation [see Bruggeman et al., 1991]. A particular category of self-excited oscillations is that related to flow instabilities that excite a resonant acoustic field, in this case the oscillations are strongly enhanced. In addition since the RPE aeroacoustic behavior is quite different with respect to rectangular open cavities that were extensively investigated in aeroacoustics [see Tam, 1976, Tam and Block, 1978, Murray

et al., 2009], the theoretical background available in literature, is not appropriate. For this reason experimental and numerical studies in the field of aerodynamic, acoustics and aeroacoustics were conducted by the author.

Recently the interest for this kind of geometries has been renewed thanks to their application in the field of combustion. In particular, RPE is a geometry selected to realize several types of trapped vortex combustors (TVCs) [see Hendricks et al., 2001, Singhal and Ravikrishna, 2011a,b]. TVC is a novel combustion strategy that utilizes the vortex trapped in the a cavity to stabilize the combustion. The main characteristics of this technology are a reduction in NO_x emission and pressure drop across the combustor chamber, high efficiency and compactness [see Hendricks et al., 2001]. For these reasons TVC promises to become the next generation of combustors. In the last years essentially three TVC generations have been developed in order to improve the performance of this novel technology. It is known that in the first two TVC generations a combustion instability occurred, due to the vortex's dynamics. This phenomenon is caused by two types of interaction: vortex-shear layer and vortex-wall interaction. The third generation, based on a RPE test rig, has been developed just to overcome this issue and to allow a wider operative range.

Although third generation TVC improves the combustion stability, much more studies are needed to reach a better comprehension of this phenomenon in enclosures. As a matter of fact several studies on the TVC have been provided recently, but no robust experimental studies focused on TVC aeroacoustic or thermoacoustic properties are available in literature [see Agarwal and Ravikrishna, 2011]. Sturgess and Hsu [1998] performed an experimental study on a first generation TVC, showing the presence of a distinct peak in the noise spectrum associated to the combustion. When this kind of noise occurred, they also observed a coupling between acoustic, heat release and flow structures generation. Besides Hsu et al. [1999], working on a first generation TVC, identified even two types of combustion instability: in the first one the flame blowout was *smooth* whereas in the second it was *abrupt* and preceded by flame intermittency and noise emission. To the best of our knowledge, there are only numerical studies on aeroacoustic and thermoacoustic of third

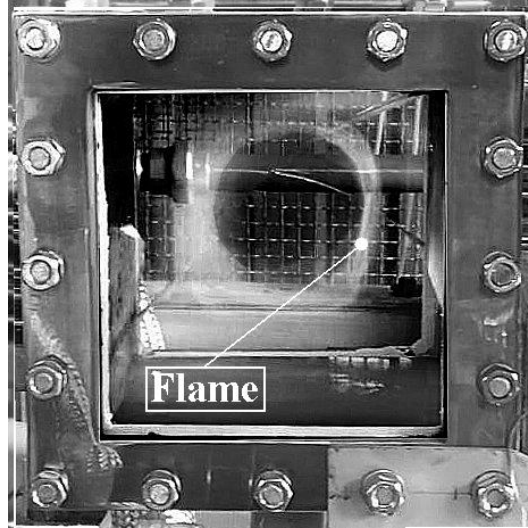


Figure 1: Picture of trapped vortex combustor based on RPE geometry realized by Italian National Agency for New Technologies, Energy and Sustainable Economic Development (ENEA courtesy).

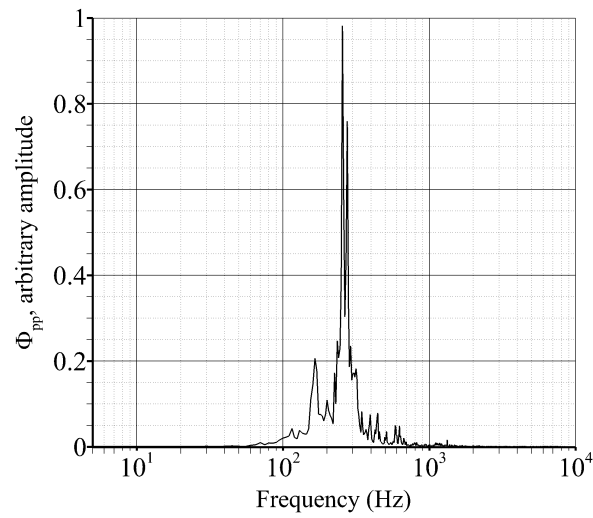


Figure 2: An example of power spectrum of the pressure fluctuation radiated from the combustor in reactive condition.

generation TVC, such as those performed by Agarwal and Ravikrishna [2011], who pointed out that the acoustic *depth-mode* is dominant in this kind of combustor and it influences the heat release. An example of TVC based on a RPE, actually under investigation by the author, is shown in Figure 1. High intensity tonal noise is radiated by this combustor for different operative conditions. In Fig. 2 an example of power spectrum computed in a reactive condition is reported. A considerable tonal component is exhibited by the combustor. Typically high intensity narrow band noise is related to thermoacoustic instability of high power combustion chambers, whereas in this case the power is very low (about 45 *kWatt*). This behaviour is due to RPE geometry that on one hand allows a single stable vortex formation in the cavity, and on the other is affected by self-excited oscillation. The application in TVC systems has driven our research but, as will be shown below, the results achieved have a more general impact.

The pressure fluctuation measurements in enclosure are quite puzzling because acoustic mode and hydrodynamic contribution, due to the large highly energetic structure, are strongly connected. The objective of the present research is to provide a complete description of the pressure fluctuations in this kind of geometry by the interpretation of the wall microphone measurements. An aerodynamic overall description is given and the main flow structures are identified. Analyses of the acoustic behaviour provided with a modal test and a numerical simulation are reported and supported by a theoretical model. Finally fluid dynamic and acoustic information are recalled to interpret the wall measurements for a wide range of parameters.

This thesis is organised as follows: a description of the theoretical acoustic model is given in (§1.1). An introduction to the proper orthogonal decomposition used to process the data are reported in (§1.2). In the next section (§1) the experimental set-up and the measurement techniques applied are presented. Subsequently an aerodynamic and acoustic characterization are illustrated in §4.2 and §4.3 respectively. Finally wall pressure fluctuations spectra and cross-correlation are reported and discussed in §4.4.

Chapter 1

Background

1.1 Acoustic model

1.1.1 Introduction

A stand-alone Helmholtz resonator (HR) is an acoustic device consisting of a cavity (volume) and a neck (opening), that are not connected to any other acoustic system. In the course of time HR has been widely studied, with various revisions to its mathematical description. In fact, since some discrepancies between experimental and theoretical results have arisen, the classical equation for HR has been modified by several authors. HR was first described in the literature by Hermann Ludwig Ferdinand von Helmholtz . He proposed the first mathematical theory for cavity resonators (volume) having a circular opening, and introduced a simple equation for calculating their resonance frequencies. This equation based on the volume of the cavity and the radius of the opening, is given by:

$$f = \frac{\bar{c}}{2\pi} \sqrt{\frac{2r}{V}}, \quad (1.1)$$

where, \bar{c} is the sound speed, r the radius of the opening and V the volume of the cavity. Later, Rayleigh presented a simplified theory for HRs, according to which, the fluid particles in the exterior domain, in close proximity to the opening, oscillating inside the neck. Therefore, an additional length

should be added to the actual length of the neck in order to include the mass loading of the fluid. This additional length is more commonly referred to as an *end-correction* [Pierce, 1994]. In particular Rayleigh made clear that two end-correction factors are needed, one for each end : an interior end-correction factor (δ_i), which corresponds to the neck-cavity interface, and an exterior end-correction factor (δ_e), which corresponds to opening face of the neck in communication with the environment. Rayleigh derived the expression for the exterior end-correction factor using the model of a circular piston radiating from an infinite baffle, assuming a constant velocity profile of the fluid over the neck cross-sectional area. The expression for exterior end-correction factor was also used to calculate the interior end-correction factor. Rayleigh developed the equation for HR resonance frequencies calculation, including the effective length of the neck, l' , in addition to the other parameters, i.e. the cavity volume and opening sectional area. The formula, which is more commonly referred to as the *classical formula* is based on the assumption that all the fluid particles in the neck oscillate at the same velocity and phase, and is given by

$$f = \frac{\bar{c}}{2\pi} \sqrt{\frac{\pi r^2}{l'} V} \quad (1.2)$$

where l' is the neck length plus the two end-correction factors. In 1953, Ingard presented a series of works about resonators investigating there behaviour for wide range of parameters. Ingard found that the application of the Rayleigh's formula for the interior end-correction determination is valid only for the the neck dimensions small compared to the dimensions of the cavity. Moreover he demonstrated that the Rayleigh formula can lead to significant errors when this condition is not satisfied. In the present work this condition is not satisfied. For this reason an acoustic lumped model has been formulated in order to predict the first mode frequency of the geometry under investigation.

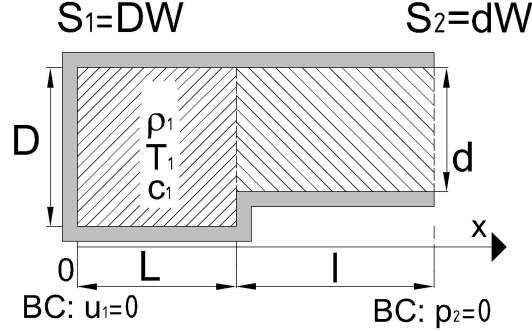


Figure 1.1: Schematic diagram of the RPE considered in quasi-monodimensional model.

1.1.2 Lumped model

The analysis of acoustic resonances in the RPE geometry analysed therein represents a fundamental task of the present investigation. In order to correctly interpret the data, the frequency of the first acoustic mode is predicted using a simple model. In this acoustic model only the propagation of plane waves is considered. This assumption is correct only when the oscillation frequency f is low that is a reasonable hypothesis when the first mode is considered. As a further assumption, the medium in the system is assumed uniform and at rest. If the Mach number, $M = U/\bar{c}$, is sufficiently low, the convective effects on the wave propagation can be neglected. In this case the error made is of the order of $O(M^2)$. An acoustic lumped model can be established by decomposing the RPE in two regions. The regions, separated by a surface discontinuity, are herein indicated as cavity and neck.

The general solution of the homogeneous wave equation can be written in the following form:

$$p'(x, t) = f(t - x/\bar{c}) + g(t + x/\bar{c}), \quad (1.3)$$

where the function $f(t)$ and $g(t)$ are arbitrary. From the linearized one-dimensional momentum equation, the velocity oscillations are obtained in

the following form:

$$u'(x, t) = \frac{1}{\bar{\rho} \bar{c}} [f(t - x/\bar{c}) - g(t + x/\bar{c})], \quad (1.4)$$

where $\bar{\rho}$ and \bar{c} are respectively the average of the density and the speed of sound. It is convenient to write Eqs. 1.3 and 1.4 using the complex formulation:

$$\hat{p}(x) = \hat{f}e^{-ikx} + \hat{g}e^{ikx}, \quad (1.5)$$

$$\hat{u}(x) = \frac{1}{\bar{\rho} \bar{c}} [\hat{f}e^{-ikx} - \hat{g}e^{ikx}]. \quad (1.6)$$

The solution of the homogeneous wave equation in the upstream region that satisfies the hard wall boundary condition, $\hat{u}_1(0) = 0$, is:

$$\hat{p}_1(x) = A \cos(kx), \quad (1.7)$$

$$\hat{u}_1(x) = -\frac{iA}{\bar{\rho} \bar{c}} \sin(kx), \quad (1.8)$$

where A is an arbitrary constant and k the wave number. The solution of the homogeneous wave equation in the downstream region that satisfies the open-end boundary condition, $\hat{p}_2(L + l) = 0$, is:

$$\hat{p}_1(x) = B \sin[k(L + l - x)], \quad (1.9)$$

$$\hat{u}_1(x) = -\frac{iB}{\bar{\rho} \bar{c}} \cos[k(L + l - x)], \quad (1.10)$$

where B is an arbitrary constant, L is the cavity length and l denote neck length. The matching between the two solutions at the location of the section discontinuity, $x = L$, is achieved by the Rankine-Hugoniot jump condition written as follows:

$$\hat{p}_1(L) = \hat{p}_2(L), \quad (1.11)$$

$$\bar{\rho}\hat{u}_1(L)S_1 = \bar{\rho}\hat{u}_2(L)S_2. \quad (1.12)$$

Eventually, using the ratio of the jump conditions, the model can be written as follows:

$$\frac{1}{\Gamma} = \tan(kL) \tan(kl). \quad (1.13)$$

Where Γ is the cavity/neck section ratio. A similar procedure has been indicated by Altay et al. [2009] to formulate a model suitable for backward facing step geometries in combustors [see Altay et al., 2010]. Eq. 1.13 was found by Tang and Sirignano [1973] and applied by Poinsot and Veynante [2005] to predict the frequency of the first acoustic mode of so-called *double duct* geometries (DD). From Eq. 1.13, we can derive resonant conditions of different geometries, such as a quarter wave tube and Helmholtz resonator (HR). Indeed, in the limiting case $\tan(kL) \rightarrow \infty$ and $l \rightarrow 0$, the one quarter wave situation is achieved:

$$\frac{\pi}{2} = kL. \quad (1.14)$$

whereas in the case of $kL \ll 1$ and $kl \gg 1$, short cavity and long neck, Eq. 1.13 can be expanded to the first order obtaining:

$$\frac{1}{\Gamma} = kL \tan(kl). \quad (1.15)$$

Eq. 1.15 is exactly the transcendental form that was found by Rayleigh and applied by Nielsen to the Helmholtz Resonator with long neck [Nielsen, 1949]. On the other hand, if $kL \gg 1$ and $kl \ll 1$ we can write:

$$\frac{1}{\Gamma} = \tan(kL)kl, \quad (1.16)$$

that is valid for long cavity and short neck. Finally, the conventional HR expression can be derived from 1.13 by considering $kL \ll 1$ and $kl \ll 1$ yielding:

$$\frac{1}{\Gamma} = k^2 L l. \quad (1.17)$$

For all these equations it is clear that the wave number depends on the neck length, the cavity length and the cavity/neck section ratio, i.e. $k = f(\Gamma, L, l)$. Figure. 1.2 summarises the geometries that can be treated by the equations above derived.

Eqs. 1.13 and 1.16 for important localized section restriction, $\Gamma > 10$, converge to Eq. 1.17, typical of HRs, as reported in Fig. 1.3. This issue was highlighted by Chanaud [1994] who performed several analytical and experimental studies on cubical HRs pointing out the small deviation of Eq. 1.16 from Eq. 1.17 in the case of a thin, small and centered orifice, in agreement with our previous considerations.

Present model is based on the open-end boundary condition, $\hat{p}_2(L+l) = 0$, which is not experimentally satisfied [Altay et al., 2009]. In order to increase the accuracy of the model, an end-correction can be introduced as follows:

$$l' = l + \delta_e + \delta_i = l + 2\delta_R, \quad (1.18)$$

where δ_e and δ_i are the exterior and interior end correction. Eq. 1.17 can be modified to obtain Eq. 1.19

$$\frac{1}{\Gamma} = k^2 L l', \quad (1.19)$$

The empirical procedure to evaluate δ_R , for the present geometry is described and discussed in the following. The results of the model will be compared with the numerical and experimental results, provided for several geometrical configuration, in order to understand if the geometries behave as HR or DD from acoustic view point.

1.2 Proper Orthogonal Decomposition

The Proper Orthogonal Decomposition (POD) is a basic statistical tool frequently applied to turbulent flows [see Berkooz et al., 1993]. The POD is

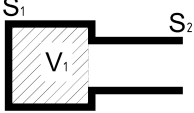
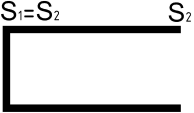
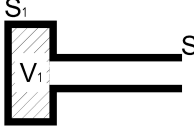
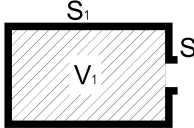
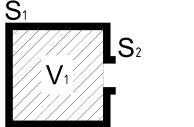
Equation	kL	kl	Diagram
<i>Double Duct</i> $\frac{1}{\Gamma} = \tan(kL) \tan(kl)$	$\gg 1$	$\gg 1$	
<i>Single Duct</i> $\frac{\pi}{2} = kL$	$\rightarrow \infty$	0	
<i>Long neck Helmholtz resonator</i> $\frac{1}{\Gamma} = kL \tan(kl)$	$\ll 1$	$\gg 1$	
<i>Long cavity Helmholtz resonator</i> $\frac{1}{\Gamma} = \tan(kL) kl$	$\gg 1$	$\ll 1$	
<i>Cubic Helmholtz resonator</i> $\frac{1}{\Gamma} = k^2 L l$	$\ll 1$	$\ll 1$	

Figure 1.2: Acoustic classification of the RPEs: representative equations, constrain conditions and sketch of the geometries.

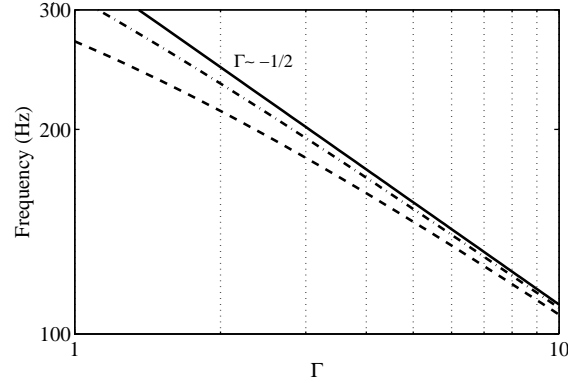


Figure 1.3: Solutions of Eqs. 1.17 (*cubical HR* —), 1.16 (*long cavity HR* · —) and 1.13 (*double duct* - - -) yield with Newton's method.

applied in this context to analyse the statistical properties of the large-scale rotating structure [see Maurel et al., 2001]. When most of the kinetic energy in the flow domain analysed by POD is embedded in a large-scale rotating structure, a common result is that low-order modes are associated to the dynamic of these structures. In this work we are interested to understand the dynamic of the structure formed both in the cavity and in the neck. In particular the recirculation bubble formed within the neck is affected by unexpected aeroacoustic behavior, as will be clarified below. As a consequence this analysis will be extended only to the neck domain.

1.2.1 The Karhunen-Loeve Decomposition

The POD is performed at the time t in a sub-domain Ω_i of the measured flow field Ω . Assuming here that the quantity $u(x, t)$ represents a scalar field, after the POD procedure application an instantaneous realization at time t_k , say $u(x, t_k)$, can be reconstructed in terms of a basis of eigenfunctions $\phi_j(x)$, which represent the modes of the ensemble:

$$u(x, t_k) = a_0 \phi_0(x) + \sum_{j=1}^{\infty} a_j(t_k) \phi_j(x), \quad (1.20)$$

where the coefficients $a_j(t_k)$ are referred to as time coefficients. The basis

in Eq. 1.28 is provided maximizing the quantity [see Berkooz et al., 1993]:

$$\frac{\langle |\langle \phi, u \rangle|^2 \rangle}{\|\phi\|^2}. \quad (1.21)$$

In Eq. 1.21 $\langle \cdot \rangle$ denotes time average or ensemble average, (\cdot, \cdot) is the inner product and $\|\cdot\|$ a norm. As a matter of fact maximization of the quantity in Eq. 1.21 can be reduced to an eigenvalue problem [see Berkooz et al., 1993]:

$$\int_{\Omega_i} \langle u(x, t) u(x', t) \rangle \phi(x') dx' = \lambda \phi(x), \quad (1.22)$$

1.2.2 Method of Snapshots

In practical applications, the domain of interest, Ω_x is discretised in a several number of points, applying the well-know method of snapshots [Sirovich, 1987]. The eigenvalue problem size is $N \times N$, where N is the number of instantaneous samples, or snapshots. This eigenvalue problem can be written as follows:

$$\tilde{C} \mathbf{A}_j = \lambda_j \mathbf{A}_j \quad (1.23)$$

where \tilde{C} is the autocovariance matrix, \mathbf{A}_j an eigenvector and λ_j the corresponding eigenvalue. The solutions are ordered according to the size of the eigenvalues:

$$\lambda_1 > \lambda_2 > \dots > \lambda_N = 0. \quad (1.24)$$

Sirovich, using ergodic theory, proposed that the autocovariance matrix can be approximated by a summation of snapshots. A clear description of the procedure adopted to obtain \tilde{C} is reported in Meyer et al. [2007]. The eigenvector calculated solving eq.1.23 make up a basis for constructing the POD modes Φ_j :

$$\Phi_j = \frac{\sum_{n=1}^N A_j^n \mathbf{u}^n}{\|\sum_{n=1}^N A_j^n \mathbf{u}^n\|}, \quad (1.25)$$

where A_j^n is the n-th component of the j-th eigenvector, \mathbf{u}^n is the vector in which n-th snapshot has been recasted and $\|\cdot\|$ denotes the discrete 2-norm.

The mode coefficient denotes a_j^n is the projection of instantaneous realization, \mathbf{u}^n , on mode j-th mode, Φ_j :

$$a_j^n = \Phi_j \cdot \mathbf{u}^n. \quad (1.26)$$

The expansion of the fluctuating part of a snapshot n is:

$$\mathbf{u}^n = \tilde{\Psi} \mathbf{a}^n, \quad (1.27)$$

where $\tilde{\Psi} = [\Phi_1 \cdots \Phi_n]$ has been introduced.

The ordering of the eigenvalues and eigenvectors in eq. 1.24 therefore ensures that the most important modes in terms of energy are the first ones. This usually means that the first modes will be associated to large-scale flow structures. If a flow has dominant flow structures, these are therefore reflected in the first POD mode. In this work about 1200 snapshots have been used for the POD computations.

1.2.3 POD limit method: time coefficients information and interlink with the statistical behaviour of the fluid field

The spatio-temporal relation between the modes and the instantaneous samples through the time coefficients is shown in Eq.1.28. Furthermore the time coefficients summarize the temporal variations of the different modes. Then it is possible to obtain the frequency spectrum of a mode performing a simple Fourier analysis of the corresponding sequence of time coefficients. This is obviously possible only if the temporal resolution is high enough, e.g. in the case of LES data or time resolved PIV. In all the other cases, when the application of the classical double shot PIV is provided, only the instantaneous realizations can be obtained. That being so in the present work the author intends to proposed a novel formulation to recast POD information obtaining a clear representation of the effect induced by each mode on average

field, as described below. Since POD is a linear expansion of instantaneous realization, can be evaluated the effect of a single mode on instantaneous velocity field superimposing to the mean field the $i - th$ mode multiplied to its coefficient $a_i(t_j)$:

$$u^i(x, t_j) = \langle u(x, t) \rangle + a_i(t_j)\phi_i(x), \quad (1.28)$$

Usually statistical parameters of the flow field, as mean velocity or turbulence kinetic energy, are very interesting, so we can consider $a_i(t)$ from a statistical view point. Assuming a normal distribution for the coefficient $a_i(t)$, we can expand it as follows:

$$u^i(x, t) = \langle u(x, t) \rangle + [\langle a_i \rangle + k_j \sigma_{a_i}] \phi_i(x), \quad (1.29)$$

where $\langle a_i(t) \rangle$ and σ_{a_i} are the mean and standard deviation of a_i . Computing Eq. 1.29 for k_j equal to ± 2 we can obtain two *limit cases* indicated as $u(x)_{\phi_1^+}$ and $u(x)_{\phi_1^-}$. Such *limit cases* define the bound of an interval that cover all the possible realizations with a probability of occurrence of about 95%. This procedure, herein called *POD limit method* or *POD_{lm}*, has been tested on database numerically provided. The dynamic of the Rankine vortex is induced superimposing different sinusoidal disturbances on radial and azimuthal component of the velocity to induce a vortex dynamic (e.g. vortex wandering, flapping, stretching) an example of perturbed Rankine vortex is defined as follows:

$$\begin{cases} u_\theta = u_\theta^M r [1 + \frac{\varepsilon}{\delta} \cos(\omega t)] & r \leq r_{ell}, \\ u_\theta = u_\theta^M \frac{\delta^2}{r} [1 - \varepsilon \frac{\delta}{r^2} \cos(\omega t)] & r > r_{ell}. \end{cases} \quad (1.30)$$

where u_θ^M is the maximum velocity occuring at the vortex core edge, ε the amplitude of the perturbation and δ is the characteristic length of the vortex. More details about the perturbed formes of the Rankine vortex equation is reported in 3.4.

POD_{lm} is applied using the instantaneous realizations numerically simulated by Eq. 1.30. All instantaneous realizations are selected using a random algorithm in order to obtain the autocovariance matrix with the neighbor columns time-independent. The statistical reconstruction provided computing POD_{lm} is quite similar with the instantaneous realizations that occur for $\omega t = \pm\pi$, namely the opposite phase of the perturbation:

$$u(x)_{\phi_1^+} = \begin{cases} u_\theta^M r [1 + \frac{\varepsilon}{\delta} \cos(\pi t)] & r \leq r_{ell}, \\ u_\theta^M \frac{\delta^2}{r} [1 - \varepsilon \frac{\delta}{r^2} \cos(\pi t)] & r > r_{ell}. \end{cases}, \quad (1.31)$$

$$u(x)_{\phi_1^-} = \begin{cases} u_\theta^M r [1 + \frac{\varepsilon}{\delta} \cos(\pi t)] & r \leq r_{ell}, \\ u_\theta^M \frac{\delta^2}{r} [1 - \varepsilon \frac{\delta}{r^2} \cos(-\pi t)] & r > r_{ell}. \end{cases}, \quad (1.32)$$

so this novel approaches can be used to obtain information about the dynamic of the flow field when the time evolution is not resolved as sometimes occurs in PIV data.

Chapter 2

Experimental set-up

Several experiments have been performed for obtaining a phenomenological overview of the self-excited pressure oscillations in RPE. In Fig. 2.6 a sketch of the test case under different flow and geometrical conditions is presented. Particular attention has been given to two geometrical conditions: $\Gamma = 3.8$, also defined *square cavity* and $\Gamma = 2.6$, indicated as *rectangular cavity*. As illustrated in the following, the cavity aspect ratio plays fundamental role in terms of flow-structure, pressure gradient, acoustic and aeroacoustic behaviour.

2.1 The experimental test case

Several prototypes have been hand-made by the author in the thermo-fluid dynamic section of the experimental laboratory of the Engineering Department of the University RomaTre of Rome. Most part of the geometry has been realized in Poly-methyl-methacrylate. Although from optical view point the performance of this material is not completely satisfactory, it is easy handling and processing at low cost, so it is selected to make the wall of the prototypes. An example of RPE wall designed and then realized is reported in Fig. 2.1.

The injection system of the RPE has been realized mounting commercial injectors and connectors (see Fig. 2.2(c) and 2.2(d)) on the RPE walls that

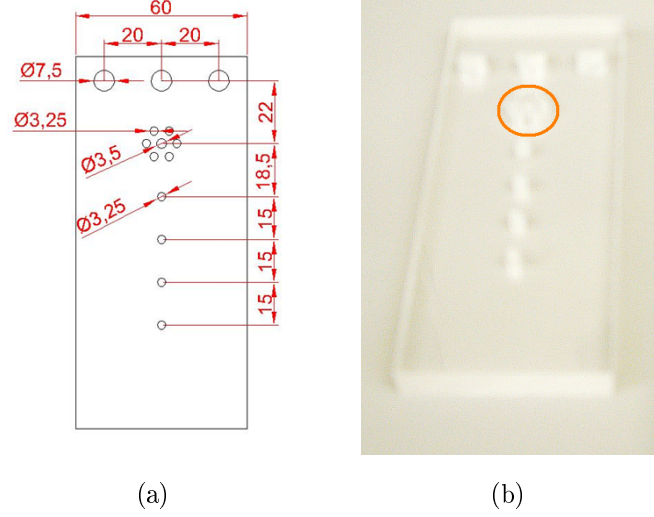


Figure 2.1: RPE forward wall project (a) and a picture of the component realized (b).

were drilled and threaded previously. For the cluster of holes, evidenced in Fig. 2.1(b) a home-made injector has been designed and made. A picture of the injection system prototype is reported in Figs. 2.2(a) and 2.2(b). In Fig. 2.3(a), 2.3(b) and 2.3(c) the pictures of the others of the test case are displayed. The completed model is obtained by recasting all parts just mentioned to realize the prototype (Fig. 2.3(d)).

Finally the pictures of two models installed in fluid dynamic laboratory for PIV measurements and in anechoic chamber for aeroacoustic tests are given in Fig. 2.4 and 2.5. The first model has three walls of black color to increase the contrast in the Mie scattering images. Such test case is fitted with an annular pipe to transport the seeding in the exterior of the laboratory. The second model, all realized in transparent material, is fitted with connectors to locate the microphones within the geometry.

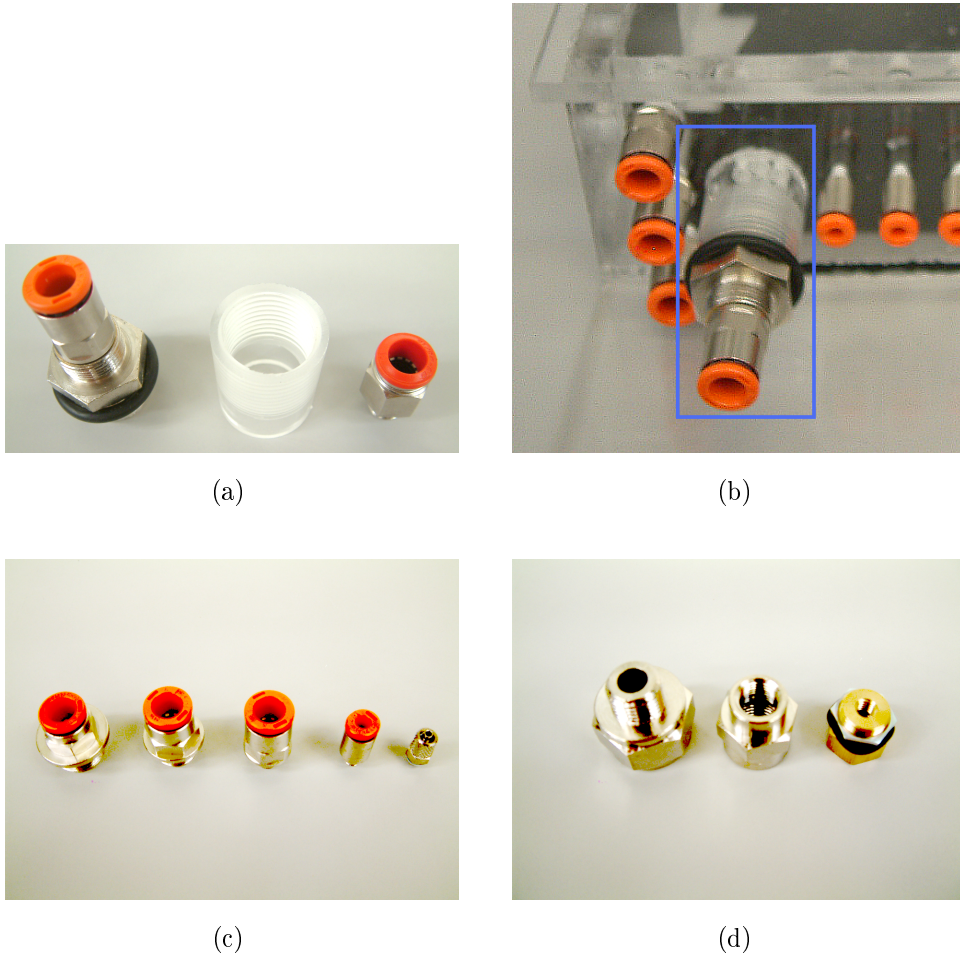


Figure 2.2: Three part of hand-make multi-whole injector (a), multi-whole injector installed on RPE (b) , some commercial injectors installed on RPE (c) and some commercial connectors used to make RPE air supply (d).

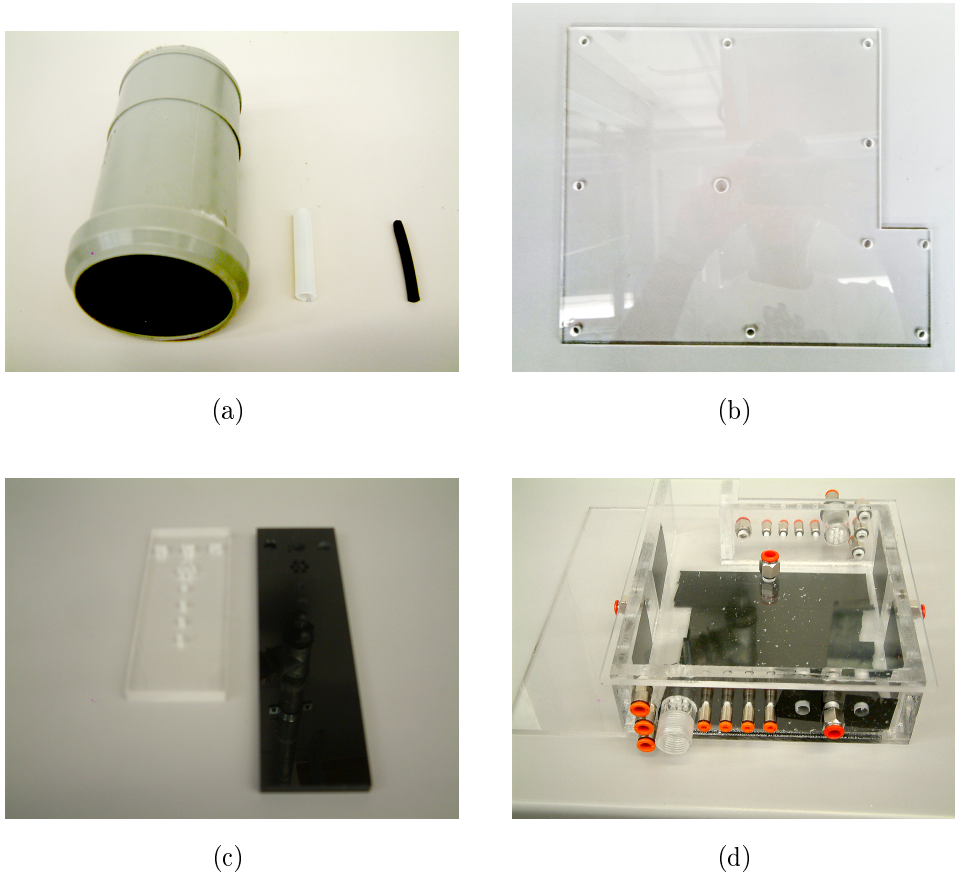


Figure 2.3: Three part of the pipes mounted on RPE (a), side wall of RPE (b), forward and backward wall of the RPE where the injection system is fitted (c) a prototype of the RPE produced (d).

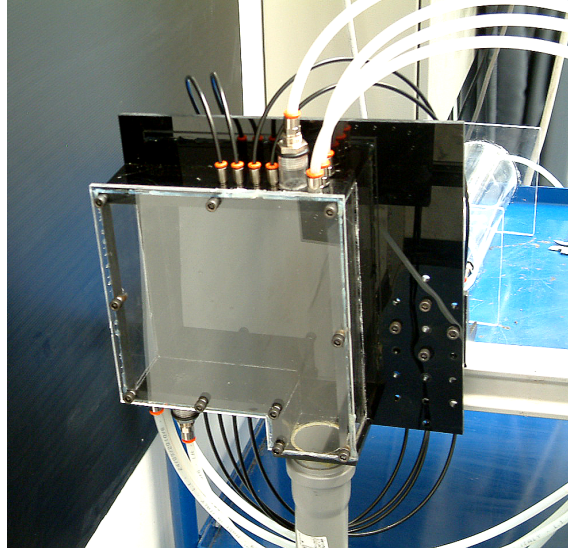


Figure 2.4: Picture of the RPE installed in the laboratory.

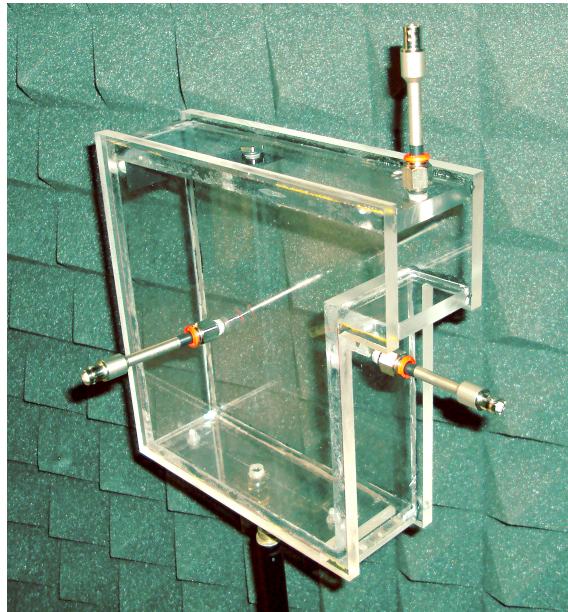


Figure 2.5: Picture of the RPE installed in the anechoic chamber.

Γ	D (mm)	L (mm)	W(mm)	l(mm)	d (mm)
$2 \div 7.3$	$100 \div 220$	190	60	50	$30 \div 50$

Table 2.1: Values of the test case geometrical parameters.

2.2 Test Case

For the RPE under consideration, the cavity length L was kept fixed and the depth D was made variable. This is accomplished by locating different plates on the cavity bottom, so that the cavity aspect ratio Γ could be changed from 2.00 to 7.3.

The number of achievable geometrical configurations is 72, but the following discussions is restricted to the most interesting cases. In table 4.2 all values assumed by geometrical parameters of the test case are reported.

The geometry analysed exhibits a width-length ratio equal to 0.33: it is well-known that, when $W/L < 1$, the vortex column formed in the TVC cavity is highly coherent in the spanwise direction so that the flow dynamics can be considered two-dimensional. This assumption has been confirmed by several RANS simulations that not reported here for brevity. The neck height, d , was varied as well between $50mm$ and $30mm$.

2.3 Air supply, collector, muffler

The experimental facility has been designed to carry out experiments at atmospheric pressure. Air supply is provided by two lines: the first one connects an high pressure plenum chamber to the test rig through a series of ball valves, pressure regulators and flow meters. The second one, denoted as *bypass* line, is connected to the seeding system of the PIV setup and it is described in the next paragraph. An air supply system is depicted in Fig. 2.12 by a single-line diagram. The flow-meter adopted is a Brooks Smart Mass Flow 5853S, that regulates the mass-flow between 1 to $15g/s$. The flow-meter is connected to a home-made *muffler-collector* very similar to the one proposed by Wu et al. [2008]. It is designed in a single-inlet/triple-

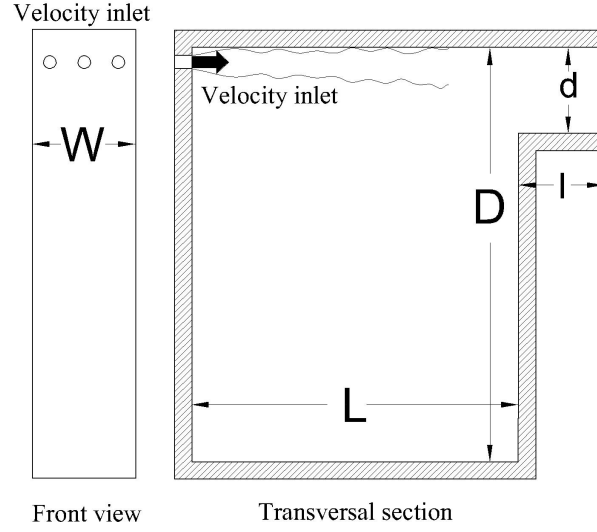


Figure 2.6: Sketch of front view and transversal section of the rectangular partial enclosure test case, reporting the main symbols using in the text.

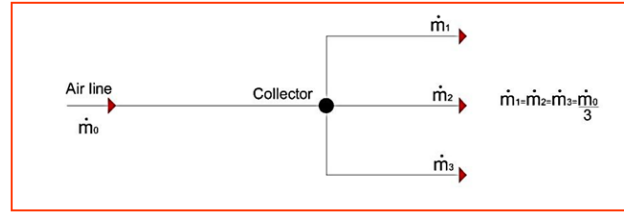


Figure 2.7: A conceptual design of a collector.

outlet configuration, to split the main mass-flow in three equivalent flows as illustrated in Fig.2.7.

The first prototype of collector realized shown in Fig. 2.8 is affected by significant pressure drop. In order to clarify this issue a Reynolds average Navier-Stokes numerical simulation of this device has been performed. A $k-\omega$ viscous model, unstructured mesh (10^6 of cells) and second order solver (both continuous and momentum equation) are used to simulate the flow field developed within the collector.

The simulation has been pointed out that the main source of the pressure loss in the collector is the toroidal vortex formed that dissipates a part of the kinetic energy of the fluid (see Fig. 2.9). Reducing the radius of the

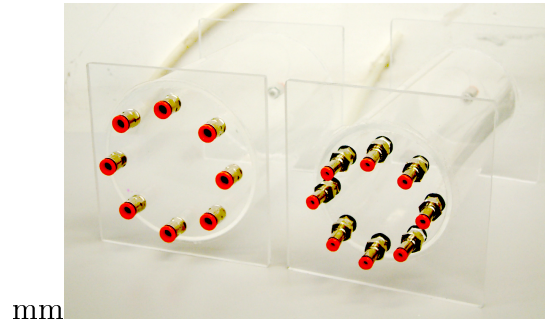


Figure 2.8: Picture of a couple of prototypes of collector.

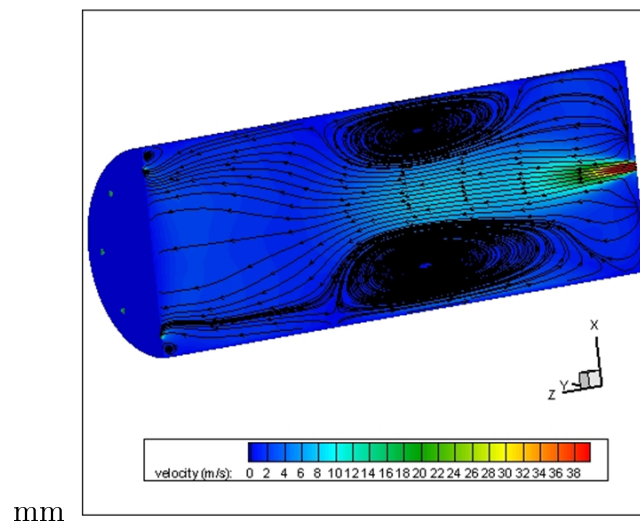


Figure 2.9: Picture of a couple of prototypes of collector.

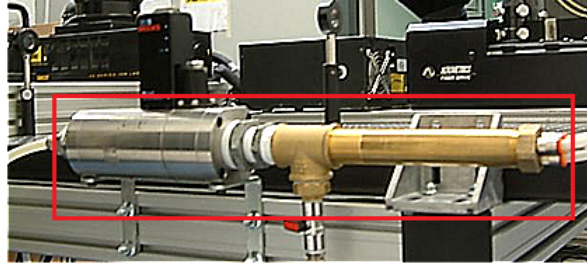


Figure 2.10: Picture of the last prototypes of muffler-collector.

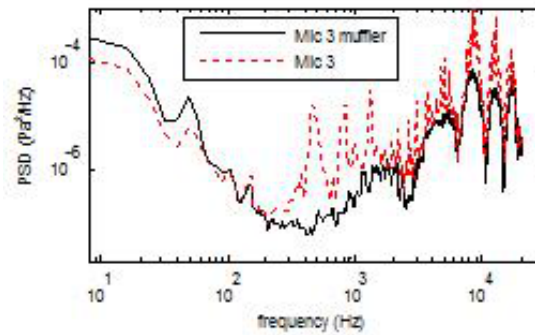


Figure 2.11: Power spectrum of the noise emitted by collector empty (red dashed line) and filled with foam (black line).

collector the pressure drop and vortex strength decrease. For this reason the last version of the collector reported in Fig. 2.10 have a diameter equal to $1/2''$.

The *muffler-collector* is filled with a foam in order to improve its acoustic absorbing property, as shown in Fig. 2.13. Several measurements have been performed to verify the mass-flow homogeneity at the collector exit and a satisfactory damping of the narrow band noise emitted by the supply system. In Fig. 2.11 an aeroacoustic test of the muffler-collector is reported. It is shown that in the frequency region from 300 Hz to 10000 Hz some peaks representative of the tonal noise occurs in red power spectrum. The effect of foam filling, with reference to black curve, is a damping of that harmonic components irradiated trough the feedline.

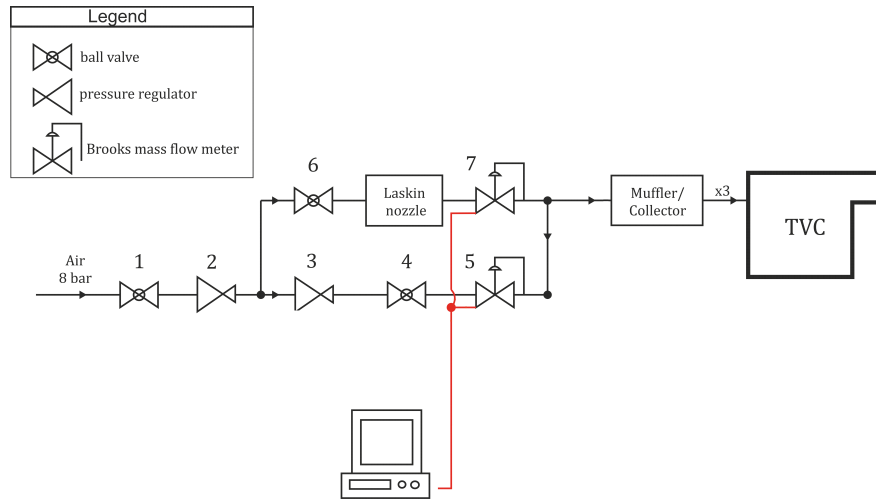


Figure 2.12: Single-line diagram of the feedline system.

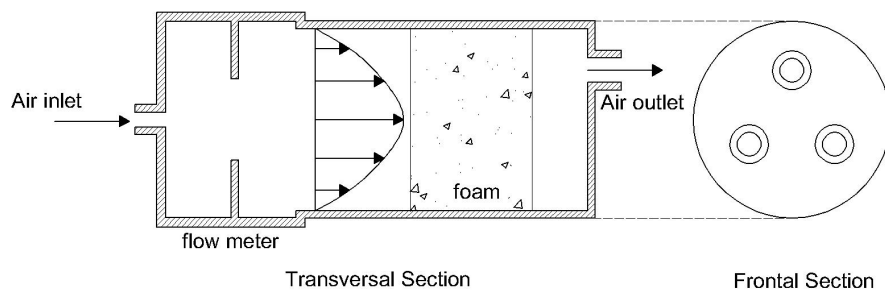


Figure 2.13: Conceptual design of the muffler-collector.

2.4 Particle Image Velocimetry

The cavity investigated has three optical accesses through top, bottom and side walls, suitable for the application of PIV measurements. A scheme of the set-up is illustrated in Fig. 2.14(a). The PIV system consists of a PCO Sensicam (double shutter camera, 1280×1024 resolution) and a 2mm thick laser sheet created by a double cavity Nd:YAG laser (200mJ light pulses). Each pair of acquired images has been processed with PIVdef, a software developed by the Italian Ship Model Basin [see Stanislas et al., 2008] that uses iterative adaptive correlation and windows deformation algorithms. The resolution of the interrogation area has been varied from 64×64 pixels to 16×16 pixels with 50% overlap. After each iteration, the vector map has been filtered to remove spurious vectors, identified by median tests and replaced using 2D interpolations. Eventually peak locking analysis, based on the displacement probability density function (pdf), has confirmed the proper setting of the final iteration. The time delay between laser pulses has been adjusted from $50\mu\text{s}$ to $150\mu\text{s}$ to provide a mean displacement vector of about 5 pixels and a velocity uncertainty of $1 - 2\%$. This accuracy is referred to all flow conditions investigated. A seeding spray of DEHS (DiEthylHexylSebacate) characterized by $1\mu\text{m}$ diameter particles has been produced by a PivTec Laskin nozzle. The seeding was mixed with the main stream air and subsequently injected into the muffler as was shown in Fig. 2.12. Essentially three fields of view (FOV) were investigated: the first one noted as FOV_1 $190 \times 190\text{mm}$ covering almost the whole cavity, the second one named FOV_2 $90 \times 90\text{mm}$ centered on the neck and the last one FOV_3 $60 \times 60\text{mm}$ centered on the top wall of the RPE, as reported in Fig. 2.14(b).

2.5 Wall pressure measurements

The symmetry plane of the RPE model was outfitted with 23 static pressure taps placed along the top wall. Starting at 10mm downstream of the RPE backward face, all pressure taps, 0.9mm of diameter were spaced 10mm apart, from center to center, in the streamwise direction, as rendered in

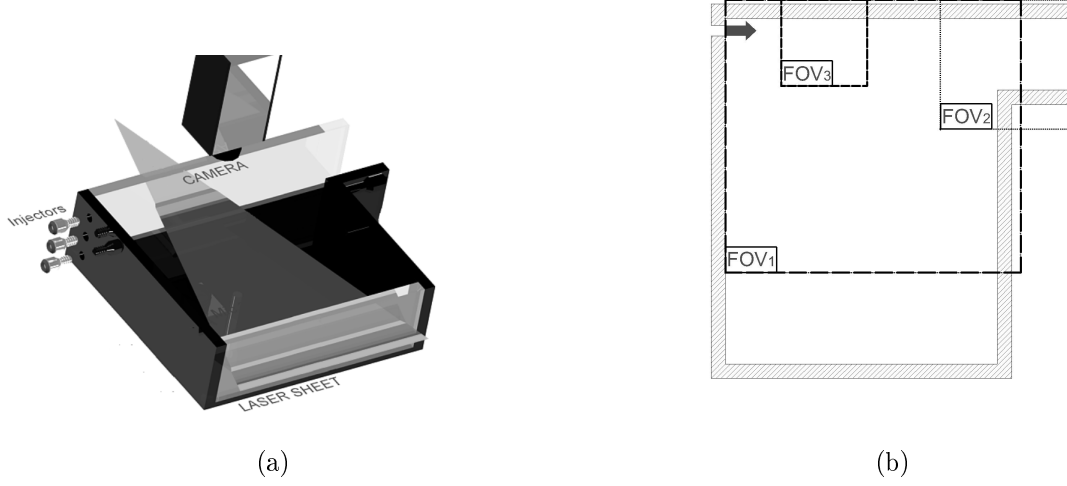


Figure 2.14: Three dimensional render of the PIV experimental set-up (a). Sketch of the three different FOV investigated.

Fig. 2.15. An Airflow TSI PVM620 series pressure transducer was used to measure differential pressure in the range $-3735Pa$ to $3735Pa$. The data are reported in term of pressure coefficient $Cp^* = (p_w - p_e)/\frac{1}{2}\rho U_{in}^2$, where p_w is the time averaged wall pressure, p_e is a reference pressure, measured at the exit of the model, U_{in} is the mean flow velocity at the inlet and ρ is the fluid density. The results are reported, considering as a reference the lenght scale $L + l$.

2.6 Modal Test

In a *stand-alone* configuration the acoustic properties of RPE have been tested in a semi-anechoic chamber. More details about that chamber can be found in Grizzi and Camussi [2012]. The test case wall has been realized with $10mm$ thickned plexiglass plates in order to satisfy the hard wall boundary condition. The test case was supported by a tripod positioned on a *sand-box* to damp the weak vibrations induced by the forcing system. A loudspeaker, preliminarily characterized, is located at $150mm$ from the outlet section, to force the acoustic modes of the test case. A sketch of this experimental set-up

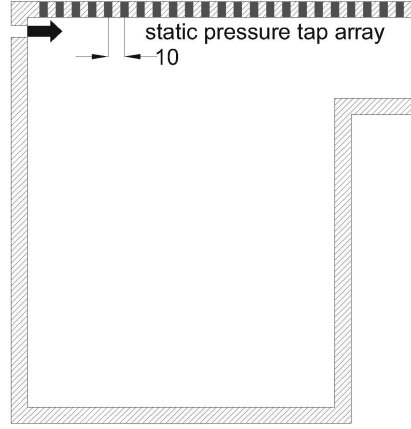


Figure 2.15: Sketch of static pressure taps realized on the top wall of the RPE.

is shown in Fig. 2.16, while a scheme of the microphone locations are given in Fig. 2.17. Microtech Gefell M360 microphones were used, four of which were flush-mounted on the wall of the cavity and one was installed stand-alone, $100mm$ far from the test case outlet section. The microphone outputs were acquired using a National Instruments A/D board with a sampling rate of $5000Hz$ per channel. The modal test has been performed by applying a swept-sine spanning from $100Hz$ to $500Hz$. The spectral response is given in terms of the FRF_{SPL} that is computed as follows:

$$FRF_{SPL} = \frac{L_{ps}^i}{L_{ps}^o} \quad (2.1)$$

where L_{ps}^o is *sound-pressure spectrum level* [Pierce, 1994] computed from the signal acquired by microphone 3, outside of the test case, whereas L_{ps}^i is referred to microphone 5 located inside the cavity as shown in Fig. 2.17. Varying D from $100mm$ to $220mm$ and d from $50mm$ to $30mm$, 36 different cavity aspect ratio have been tested to analyse the dependence of the first mode frequency upon Γ .

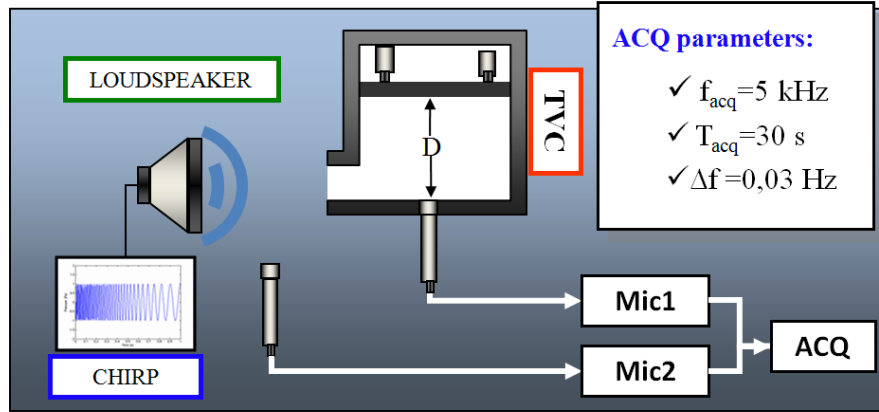


Figure 2.16: A conceptual render of the modal test.

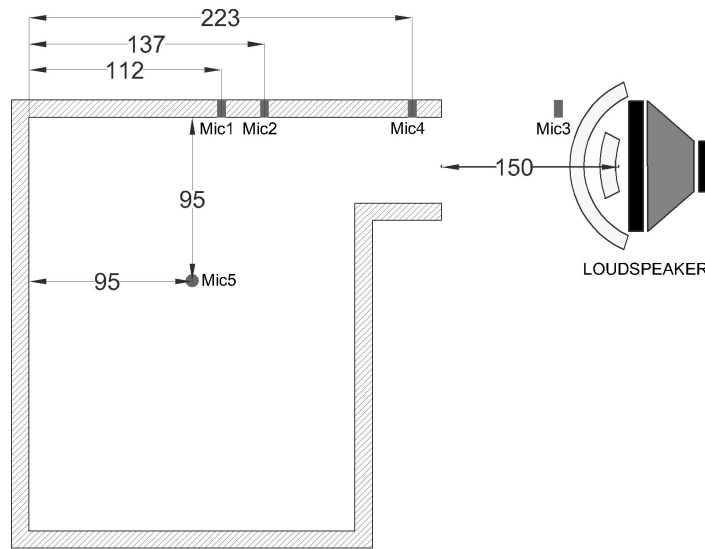


Figure 2.17: Sketch of modal test set-up.

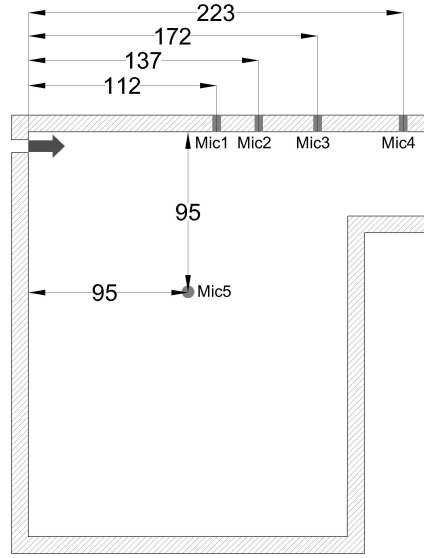


Figure 2.18: Sketch aeroacoustic experimental set-up.

2.6.1 Aeroacoustic measurements

Aeroacoustic measurements were performed for several mass flow inlet. The measurement chain is the same adopted for the modal test. The four microphones were flush mounted at a wall, as illustrated in Fig. 2.18. The data were sampled at $12kHz$ for 60s with the antialiasing cutoff frequency filter set at $5kHz$. The mass flow inlet was varied between $7g/s$ and $15g/s$ and Γ from 2.0 to 4.4. A total number of 36 configuration have been tested in this case.

Chapter 3

A single-vortex model for POD assessment

3.1 Aim

The spirit of the analysis reported in this chapter is to provide a simple tool for physical insight into single flow structure dynamic. Further, although the simplicity of a two dimensional model developed and its limitations on the accuracy, comparison between experiments and computations gives confidence that the model can be a useful representation of many aspects of vortex core flows dynamic. This study has been the first step to give an interpretation of the POD modes obtained perturbing a single Rankine vortex firstly then by means of experimental measurements. As matter of fact the physical interpretation of the POD modes is not easy to give, hence a simulation of the single perturbed vortex allows to correlate the perturbation and the dynamic of the vortex with the corresponding POD mode.

3.2 Introduction

The study of fluid motions is of obvious importance for several applications ranging in scale from the microscopic to the atmospheric. Since *we live in a three-dimensional world*, it may be less obvious why the understanding of

two-dimensional fluid flows is of interest. However, in many applications the fluid domain is much smaller in one direction than in the other two. In the case of the atmosphere for example, the flow structures thickness is a few tens of kilometers and the relative diameter can be several hundreds of kilometers. Furthermore, in both the atmosphere and the ocean, the applicability of a two-dimensional approximation is enhanced by two additional effects: the stratification of the medium (which reduces the effective thickness of the domain) and the rotation of the earth, which tends to reduce variations in the vorticity field with height, so in any cross-sectional plane the flow is effectively two-dimensional.

A single two-dimensional vortex is also an interesting feature of many technological flows. A well-known example is indeed the vortex formed in the cavities of the rectangular trapped vortex combustors. The wall-vortex interaction in a confined domain is expected to be significant and would lead to a large-scale precession even for an isolated vortical structure [Maurel et al., 2001]. In this situation, as well as in many others (e.g. in a compressor, pump or duct/neck), the central element is a vortex subjected to a pressure gradient. The possible consequence of large expansion of the vortex core is a decreasing of effective flow area, such as the performance of the enclosure. A two-dimensional approximation to the fluid motion can provide very accurate insights into the behavior of the physical system.

A particular behaviour of two dimensional flow is about turbulent kinetic energy transfer. Typically in three-dimensional flows the from large-scale is transferred to small ones until it is dissipated by the viscosity forces. In two dimensions the phenomenon tends to reverse itself and the energy concentrates itself in a few large structures. This phenomenon, known as the inverse cascade, manifests itself in a striking visual way through the coalescence of many small vortices into a smaller number of larger vortices.

3.3 Rankine vortex

The flow that we are going to describe herein is a Rankine vortex core, surrounded by an irrotational flow. The Rankine vortex is a fluid flow having

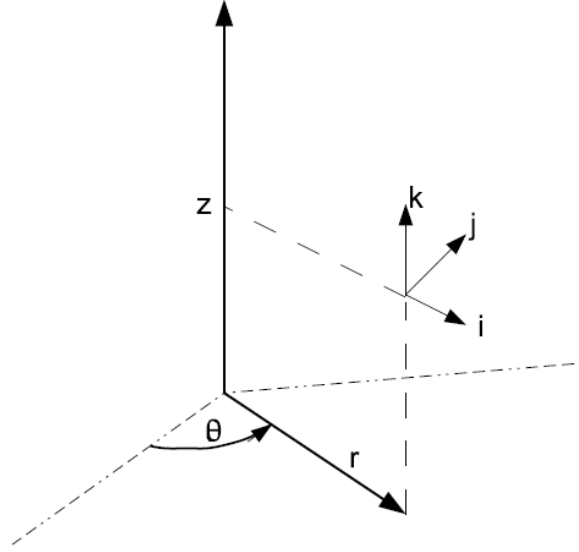


Figure 3.1: The cylindrical coordinate system adopted for the description of the Rankine vortex model. The unit normal vectors set $(\mathbf{i}, \mathbf{j}, \mathbf{k})$ is reported in the point identified by coordinates (r, θ, z) .

radial symmetry [?]. Its definition exhibits a simple form in a cylindrical coordinate system (r, θ, z) , where the symmetry axis is the z coordinate, while the r and θ axis lie on the plane normal to the z axis, as shown in Fig. 3.1.

The vortex has the velocity field normal to both the symmetry axis z and the radial vector \mathbf{r} . This means that the velocity is parallel to the \mathbf{j} unit vector. The velocity vector modulus is a function of the radial distance only. The inner part of the vortex is in solid body rotation, then its modulus is linearly proportional to r , while the outer part is inversely proportional to the radial distance. The maximum intensity of the flow is reached at the characteristic length of the vortex, δ , where there is the change from the inner linear behavior to the outer hyperbolic one. The vortex core centre is aligned with the origin of axis. Analytically the velocity in a Rankine vortex is defined as follows:

$$\mathbf{V} = v_r \mathbf{i} + v_\theta \mathbf{j} + v_z \mathbf{k} \text{ where } \begin{pmatrix} v_r = 0 \\ v_\theta(\theta, r) = \begin{cases} \frac{\Gamma_\infty r}{2\pi\delta^2}, & r \leq \delta \\ \frac{\Gamma_\infty}{2\pi r}, & r > \delta, \end{cases} \\ v_z = 0 \end{pmatrix} \quad (3.1)$$

benig the far-field circulation, Γ_∞ , constant. The maximum velocity oc-
curing, at the core edge, is defined as

$$v_\theta^M = \frac{\Gamma_\infty}{2\pi\delta}. \quad (3.2)$$

So we can rewrite Eq. 3.13 in term of v_θ^M obtaining

$$\mathbf{V} = v_r \mathbf{i} + v_\theta \mathbf{j} + v_z \mathbf{k} \text{ where } \begin{pmatrix} v_r = 0 \\ v_\theta(\theta, r) = \begin{cases} v_\theta^M \frac{r}{\delta} & r \leq \delta \\ v_\theta^M \frac{\delta}{r} & r > \delta \end{cases} \\ v_z = 0 \end{pmatrix} \quad (3.3)$$

The v_θ vector component behavior is illustrated in Fig. 3.2

One of the main features of the Rankine vortex is its vorticity field. In fact, according to the definition of the vortex velocity field and the application of the curl operator in cylindrical coordinates, it is evident that the vortex presents a vertical vorticity component only. Furthermore in the inner part

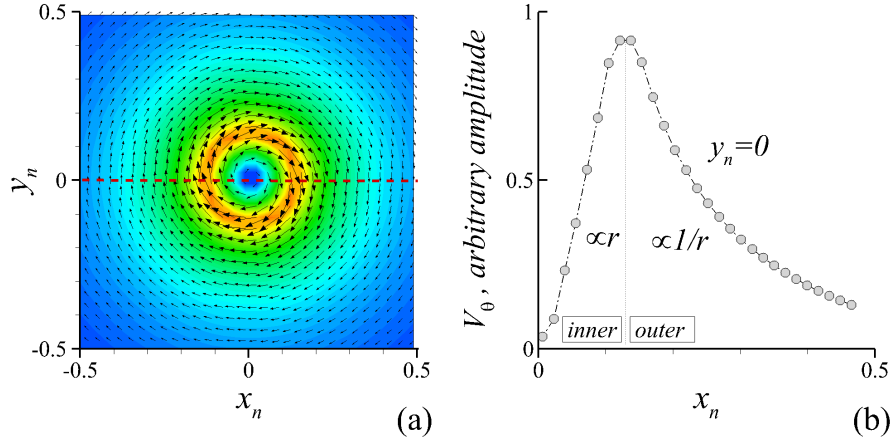


Figure 3.2: The Rankine vortex model is characterized by a flow that is always and everywhere parallel to the \mathbf{j} unit vector, so the only non null vector component is v_θ which is also the total velocity vector modulus. Note that at the characteristic length δ , the flow is continuous, but the flow regime changes from a solid rotation to a hyperbolic decrease for increasing distances.

of the vortex the vorticity field modulus is constant and positive. In the outer region of the vortex, the flow has no vorticity at all (Eq.3.4).

$$\nabla \times \mathbf{V} = \omega_z \mathbf{k} = \frac{1}{r} \frac{\partial(rv_\theta)}{\partial r} \mathbf{k} = \left(\frac{v_\theta}{r} + \frac{\partial v_\theta}{\partial r} \right) \mathbf{k} = \mathbf{k} \begin{cases} 2 \frac{v_\theta^M}{\delta} & \text{if } 0 \leq r < \delta \\ 0 & \text{if } r > \delta \end{cases} \quad (3.4)$$

It is worth noting that the Rankine vortex is characterized by a continuous velocity field, but with a discontinuity in the vorticity at the characteristic distance [Batchelor, 1993].

3.4 The vortex perturbations analysis

A Rankine vortex is perturbed superimposing different time-dependent disturbances in order to simulate its actual dynamic. An extensive description of all perturbations is given below. As illustrated by Lamb [1932], the sim-

plest case of an elliptical streamline can be constructed by superimposing on a Rankine vortex a disturbance with a small amplitude ε and wave number two (wave number two disturbance WTD).

$$\begin{cases} \psi = -\frac{v_\theta^M}{2}[(\delta^2 - r^2) - \varepsilon \frac{r^2}{\delta} \cos(2\theta - \omega t)] & r \leq r_{ell} \\ \psi = -\frac{v_\theta^M}{2}[(2\delta^2 \ln \frac{\delta}{r}) - \varepsilon \frac{\delta^3}{r^2} \cos(2\theta - \omega t)] & r > r_{ell} \end{cases} \quad (3.5)$$

where $r_{ell} = \delta + \varepsilon \cos(2\theta - \omega t)$ is the elliptical boundary of maximum velocity. This equation represents the general form of the streamfunction for WTD. In this simple analytic case, the vorticity gradient is zero everywhere except at δ . It is a straightforward matter to derive the azimuthal and radial velocities of this system from Eq. 3.5, as shown in the following:

$$\begin{cases} v_\theta = \frac{\partial \psi}{\partial r} = v_\theta^M r [1 + \frac{\varepsilon}{\delta} \cos(2\theta - \omega t)] & r \leq r_{ell}, \\ v_\theta = \frac{\partial \psi}{\partial r} = v_\theta^M \frac{\delta^2}{r} [1 - \varepsilon \frac{\delta}{r^2} \cos(2\theta - \omega t)] & r > r_{ell}, \end{cases} \quad (3.6)$$

The magnitude of the tangential velocity of the idealized WTD is continuous across r_{ell} . As a result, the WTD manifests itself as two pairs of counter-rotating vortices. If one superimposes this disturbance on the Rankine vortex, then the resulting total circulation is an ellipse varying its axis length in time. In Fig. 3.3(a, b, c) the velocity magnitude of instantaneous realization obtained for ωt equal to $-\pi$, 0 and π are reported. It is noticeable for $\omega t = -\pi$ a contraction of the vortex along $y_n - axis$ and at the same time a vortex dilatation along $x_n - axis$. By simplifying Eq.3.6, keeping the wave number of the perturbation equal to zero, it is possible to simulate a more simple disturbance, that consists of an isotropic dilatation/contraction. Such a perturbation can be modeled as follows:

$$\begin{cases} v_\theta = \frac{\partial \psi}{\partial r} = v_\theta^M r [1 + \frac{\varepsilon}{\delta} \cos(\omega t)] & r \leq r_{ell}, \\ v_\theta = \frac{\partial \psi}{\partial r} = v_\theta^M \frac{\delta^2}{r} [1 - \varepsilon \frac{\delta}{r^2} \cos(\omega t)] & r > r_{ell}. \end{cases} \quad (3.7)$$

A pure deformation field in cartesian coordinates, is another perturbation taken into account. This field can be constructed as follows [?]:

$$\begin{cases} u = \frac{D}{2} [x \cos(2\gamma) - y \sin(2\gamma)] \\ v = \frac{D}{2} [x \sin(2\gamma) + y \cos(2\gamma)] \end{cases} \quad (3.8)$$

where D is the magnitude of the deformation, measured in s^{-1} , γ is the angle of the axis of dilation, x and y are the distance from the stagnation point of the deformation field. A pure deformation field is neither rotational nor divergent and the magnitude of the velocity increases linearly with the radius. The similarities between the wavenumber two tangential wind and the deformation field case can be illustrated as follows. Representing v_θ and v_r in terms of cartesian variables u and v , it can be shown that the deformation field exhibits a WTD characteristics in cylindrical coordinates:

$$\begin{cases} v_\theta = v \cos \theta - u \sin \theta, \\ v_r = u \cos \theta + v \sin \theta, \end{cases} \quad (3.9)$$

using the well-known relations $x = r \cos \theta$ and $y = r \sin \theta$ in Eq. 3.8, then substituting the results into Eq. 3.9, and utilizing the trigonometric identities $\sin 2\phi = 2 \sin \phi \cos \phi$ and $\cos 2\phi = \cos^2 \phi - \sin^2 \phi$, we obtain:

$$\begin{cases} v_\theta = -\frac{Dr}{2} \sin(2\theta - 2\gamma), \\ v_r = \frac{Dr}{2} \cos(2\theta - 2\gamma). \end{cases} \quad (3.10)$$

Hence v_θ and v_r signatures of a deformation field are WTD and are continuous for any radius value.

The last disturbance defined is a perturbation of the Rankine vortex core position, in order to simulate an oscillation of amplitude η around the axis center, along x - *axis*. It is possible to rewrite only the radius expression to represent this disturbance:

$$\hat{r} = \sqrt{(r \cos \theta + \eta \cos(\omega t))^2 + (r \sin \theta)^2}, \quad (3.11)$$

by replacing this expression in the Rankine vortex model, an expression of the perturbed vortex is given:

$$v_\theta = \begin{cases} \frac{\Gamma_\infty \hat{r}}{2\pi \delta^2}, & \hat{r} \leq \delta \\ \frac{\Gamma_\infty}{2\pi \hat{r}}, & \hat{r} > \delta, \end{cases} \quad (3.12)$$

In Fig. 3.3(d, e, f) the velocity magnitude of the instantaneous realizations perturbing the Rankine vortex with the disturbance shown in Eq. 3.11 obtained for ωt equal to $-\pi$, 0 and π are reported. It is noticeable that for $\omega t = -\pi, \pi$ a rigid translation of the vortex along x_n - *axis* occurs.

A novel more general expression of the Rankine perturbed vortex can be derived including all disturbances illustrated.

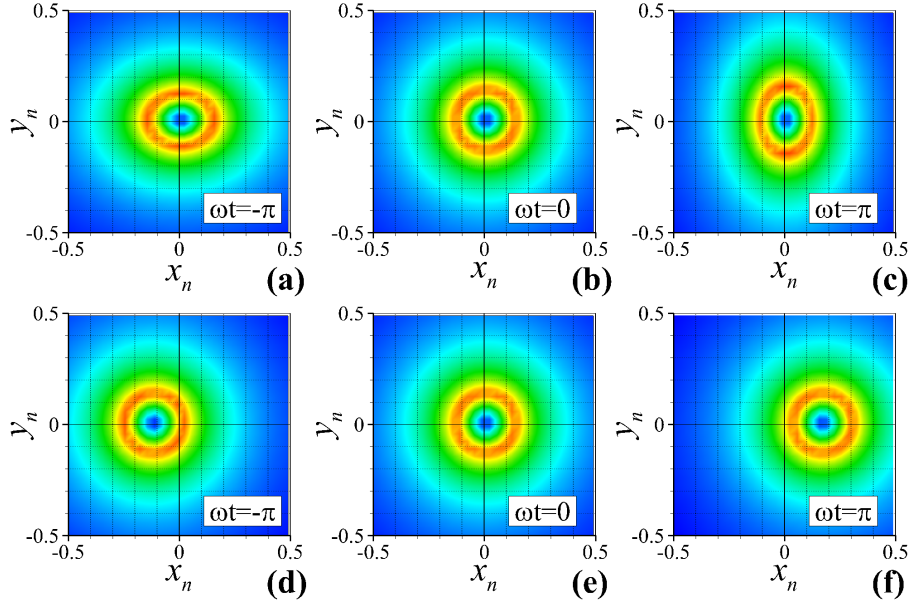


Figure 3.3: Instantaneous pictures of velocity realizations for $\omega t = -\pi$, $\omega t = 0$ and $\omega t = \pi$ (from left to right). The Rankine vortex dynamic is provided by superimposing WTD on f_θ (figures a, b, c) and perturbing the vortex core position with the disturbance \hat{r} (figures d, e, f).

$$\left(\begin{array}{l} v_r(\theta, r) = \begin{cases} -v_\theta^M \hat{r} \left(\frac{\Im(\tilde{\varepsilon})}{\delta} \right), & \hat{r} \leq \delta + \Re(\tilde{\varepsilon}) \\ -v_\theta^M \frac{\delta^2}{\hat{r}} \left(\Im(\tilde{\varepsilon}) \frac{\delta}{\hat{r}^2} \right) & \hat{r} > \delta + \Re(\tilde{\varepsilon}), \end{cases} \\ v_\theta(\theta, r) = \begin{cases} v_\theta^M \hat{r} \left(1 + \frac{\Re(\tilde{\varepsilon})}{\delta} \right), & \hat{r} \leq \delta + \Re(\tilde{\varepsilon}) \\ v_\theta^M \frac{\delta^2}{\hat{r}} \left(1 + \Re(\tilde{\varepsilon}) \frac{\delta}{\hat{r}^2} \right) & \hat{r} > \delta + \Re(\tilde{\varepsilon}), \end{cases} \\ v_z = 0 \end{array} \right) \quad (3.13)$$

where $\tilde{\varepsilon} = \varepsilon e^{(m\theta + nr - \omega t)}$ is the complex wave notation of the perturbations, sometimes called Kelvin waves, m and n are the azimuthal and radial wave number and $\Re(\cdot)$, $\Im(\cdot)$ the real and imaginary part of complex number.

3.5 Single vortex POD analysis

In this section the vortex dynamic will be simulated superimposing at same time three different perturbations to the Rankine vortex. The vortex dynamic so obtained will be analysed applying the POD technique. Since the perturbation expression are known the interpretation of the corresponding modes will be easier. As a matter of fact the main drawback of this processing technique is the physical interpretation of the modes. The home-made software used to perform such a POD analysis (*easyPOD*, illustrated in A.4.2) has been previously validated.

The amplitude of the perturbations superimposed to the Rankine vortex satisfies the condition $\varepsilon_1 \gg \varepsilon_2 \gg \eta \gg \varepsilon_3$. Where ε_1 is the amplitude of the tangential WTD, η is the amplitude of the disturbance of the vortex core position, ε_2 is the amplitude of a perturbation with zero- wave number and ε_3 is the amplitude of radial and tangential WTD. This condition is given in order to identify the corresponding mode using the eigenvalue spectrum, indeed it is expected that λ_1 , associated to the perturbation ε_1 , is higher than λ_2 that corresponds to η and so on.

The perturbation defined as $\tilde{\varepsilon}_1$ induces in a vortex a contraction/dilatation along the $x/y - axis$, a dynamic also called vortex flapping. The perturbation \hat{r} induces the variation of the vortex core location, the so called vortex wandering. Finally the disturbance $\tilde{\varepsilon}_2$ is a deformation field that induces its maximum effect when the vortex is in close proximity to boundaries of the domain, modeling the wall–vortex interaction. Such a dynamic is also denoted as vortex bouncing. It is interesting to observe the intrinsic coupling between the disturbances $\tilde{\eta}$ and $\tilde{\varepsilon}_2$, indeed the effect of the latter perturbation is a function of the vortex position that is varied by $\tilde{\eta}$.

In Fig. 3.4 the modes distilled by means of the POD are shown. Mode 0 corresponds to the mean velocity field, that is the unperturbed Rankine vortex (see Fig. 3.4 (b)). In the two dimensional field, referred as mode 1, a couple of counter-rotating coaxial structures with wave number two on v_θ components occurs, in agreement with the effect of the perturbation $\tilde{\varepsilon}_1$ (see Fig. 3.4 (c)).

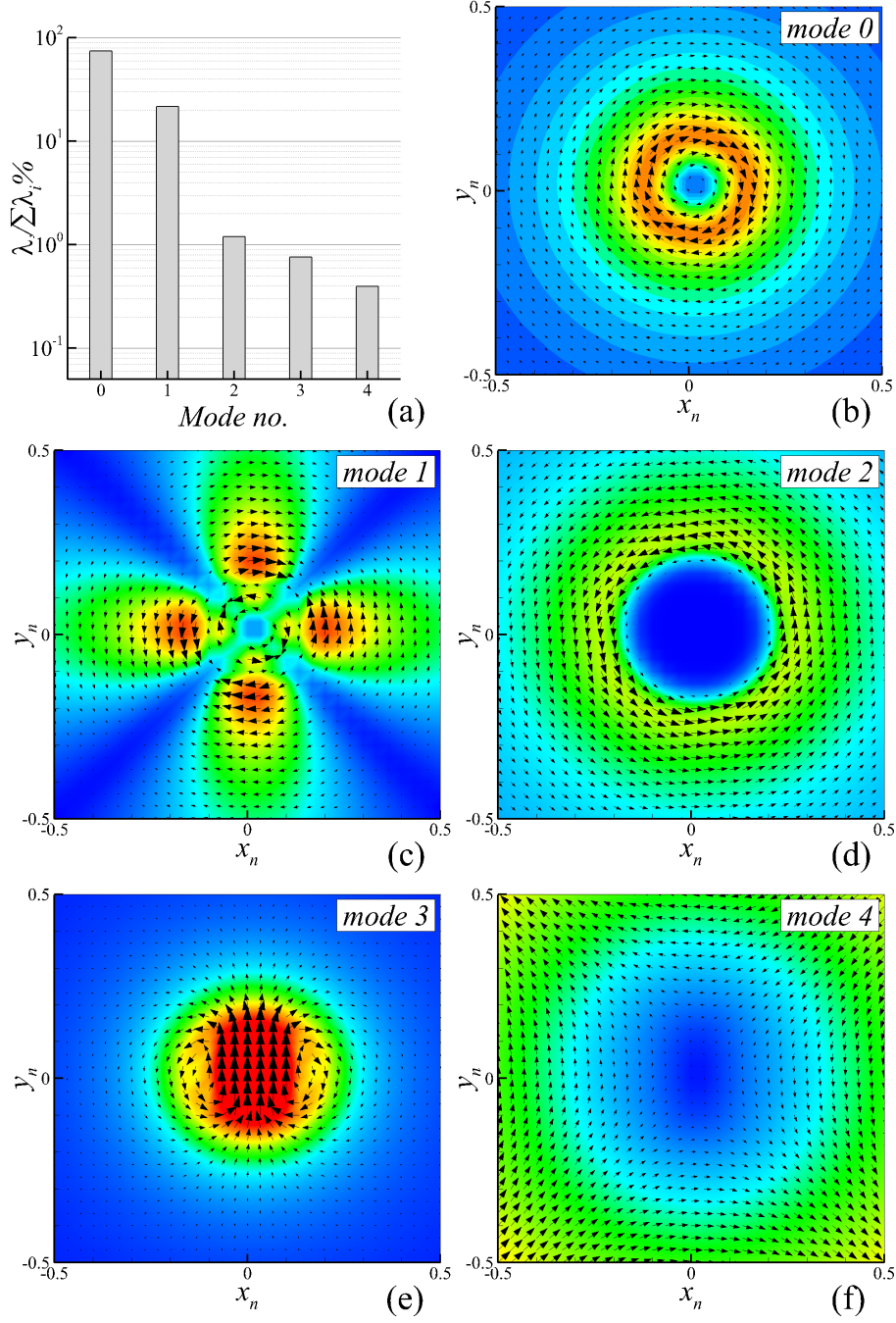


Figure 3.4: Fluctuating energy spectrum of the first four modes extracted by POD (a); Proper orthogonal decomposition modes identified by decomposition of the Rankine vortex dynamic simulation: mode 0, 1, 2, 3, 4, respectively corresponding to mean field (a), vortex asymmetric flapping (b), isotropic flapping, wandering, bouncing.

Mode 2 is a single azimuthal perturbation rotating in anti-clockwise direction with a circular stagnation region (see Fig. 3.4 (d)). Mode 3 consists of a vortex dipole that induces a flow characterized by parallel velocity vectors in the y direction, that produces a vortex wandering in transversal direction (see Fig. 3.4 (e)). Mode 4 is a deformation field with a stagnation point located at the origin in agreement with the effect of the perturbation $\tilde{\varepsilon}_2$ (see Fig. 3.4 (f)). Such a mode represents the vortex bouncing dynamic. The POD spectrum of the first four modes evidences a significant difference between the fluctuating energy of the modes, $\lambda_i / \sum \lambda_i$, in agreement with the condition on the disturbance amplitude: $\varepsilon_1 \gg \varepsilon_2 \gg \eta \gg \varepsilon_3$ (see Fig. 3.4 (a)). As a result the equivalence between perturbation linearly superimposed and mode extracted is verified, although, as said previously, an intrinsic coupling between $\tilde{\varepsilon}_2$ and η exists.

The procedure described can be considered an approach to give a physical interpretation of the modes extracted using POD by a single simulated vortex. In effect is not easy to clarify the link between vortical structure contained in instantaneous two-dimensional fields and their Proper Orthogonal modes. In this approach for all perturbation modeled the corresponding mode is recognized. Moreover the knowledge acquired in this preliminary work it is demonstrated useful to give an interpretation of modes computed from experimental database as discussed in the §4.2.1.

Chapter 4

Results

4.1 Introduction

As described above, aerodynamic, acoustic and aeroacoustic measurement were performed for different test cases. The aerodynamic characterization provides an overall picture of the main flow structures forming in the cavity. The results of the acoustic analysis are supported by specific numerical simulations and are of importance for the interpretation of the aeroacoustic investigations.

4.2 Fluid dynamic characterization

A simplified sketch of the RPE flow physics is represented in Fig. 4.1. For all Γ analysed the most important flow structures have been identified: a jet, a jet-wall interaction region, a main vortex, a recirculation bubble formed into the neck, a stagnation point. As described in §2.4, in order to describe with suitable spatial resolution all these elements, specific FOVs are selected for the PIV measurements.

The first result provided is that the fluid dynamic of this kind of geometry is affected by Γ . A variation of the cavity aspect ratio from 2.6 to 3.8 induces a vortex core displacement only in the longitudinal direction, whereas no effects occur in the transversal direction. Indeed the vortex core remains

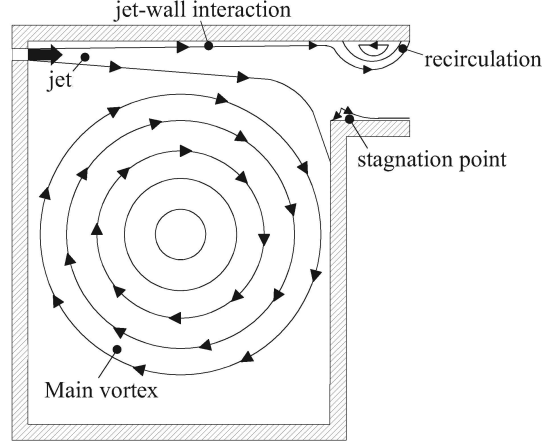


Figure 4.1: Sketch of the flow physics.

positioned in the middle of the cavity. For $\Gamma = 2.6$ a noticeable effect in the flow domain is the decrease of the azimuthal component of the velocity, V_θ (see Fig. 4.2 (a) and (b)), except for the region in the right side of the cavity. This behaviour is clarified by observing Fig.4.2 (c) and (d) where for $x > 85mm$ and $x > 110mm$ respectively the $\partial V_\theta / \partial x$ is qualitatively the same and a non zero radial velocity is induced. This behaviour can be ascribed to a jet roll-up. On the other hand, for $x < 110$ and $\Gamma = 2.6$, a remarkable V_θ decrease is noticeable. Moreover for $\Gamma = 3.8$ the V_θ has an axisymmetric distribution with respect to the center of the vortex, exhibiting a linear increase with the distance calculated from the vortex center. It is a proper approximation to consider this vortex a solid body rotation. The azimuthal velocity is very important in the trapped vortex combustion strategy, since it improves the mixing and the main vortex stability into the cavity [Bruno and Losurdo, 2007]. These observations qualitatively suggest that an optimal geometry for the experimental investigation in reactive condition is the square cavity. Singhal and Ravikrishna [2011a] experimentally investigated in reactive condition a geometry very similar to the present one, and indicated high efficiency for $L/D = 0.88$, namely about a square cavity.

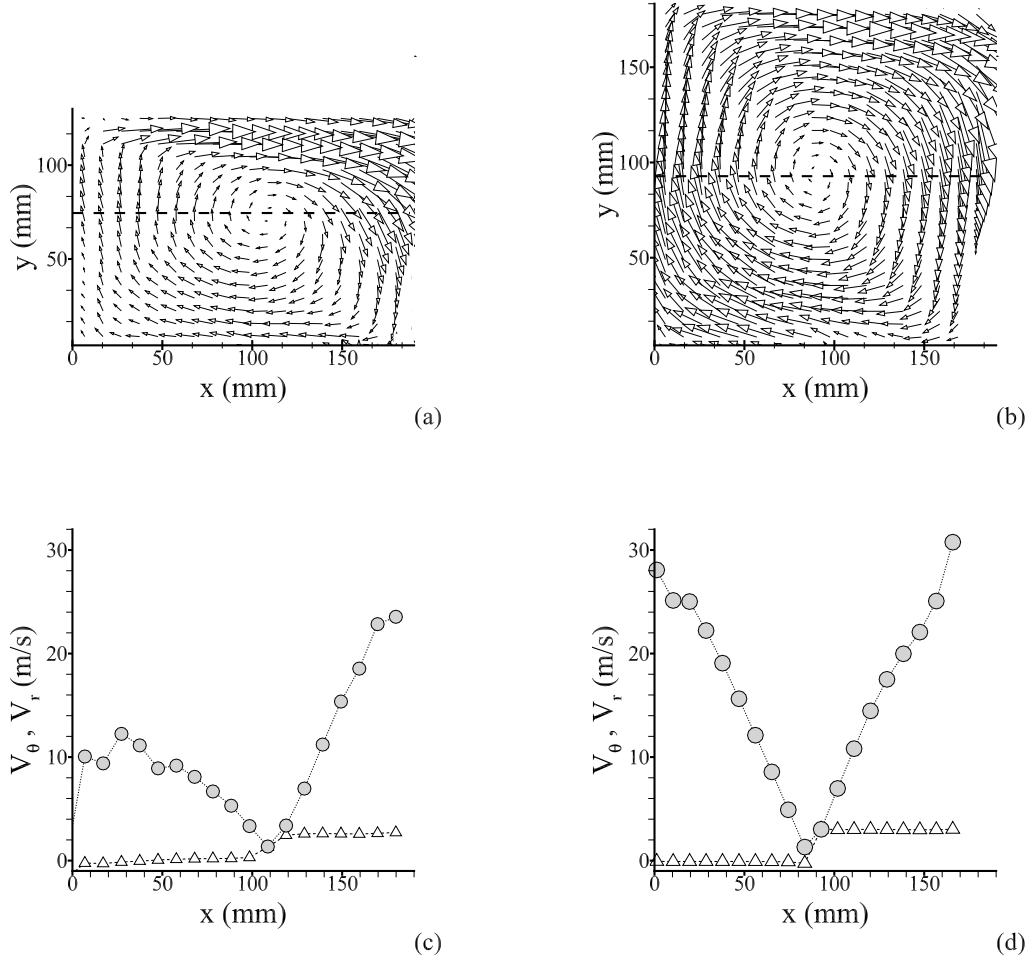


Figure 4.2: Averaged velocity field measured at $Re = 50271$ for different values of cavity aspect ratio: $\Gamma = 2.6$ (a), $\Gamma = 3.8$ (b). Azimuthal (\circ) and radial (Δ) velocity profiles extracted from the PIV data at $y = 73\text{mm}$ for $\Gamma = 2.6$ (c) and at $y = 90\text{mm}$ for $\Gamma = 3.8$ (d)

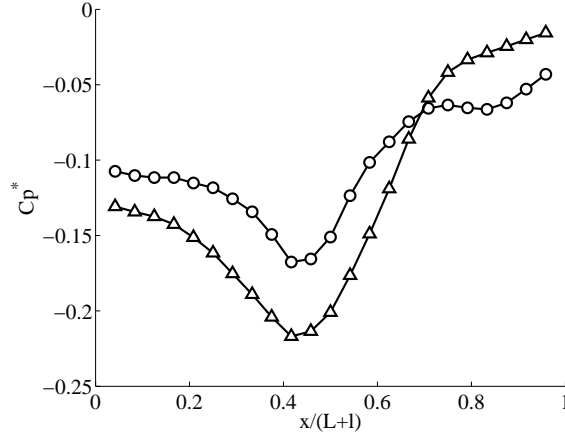


Figure 4.3: Pressure coefficient distribution along the top wall of the RPE.

An interesting feature consists in the formation of a recirculation bubble in the neck. This effect is due to the adverse pressure gradient (APG) and it is observed for all the cases under consideration. The length scale and position of this structure is affected by Γ , on which depends the APG intensity.

With reference to Fig. 4.3, it is shown that the largest pressure gradient occurs for large Γ , where a wider separation zone is observed as well, as illustrated in Fig. 4.4. In this Figure it is noticeable that the stagnation point is weakly displaced upstream for the case with $\Gamma = 2.6$. In summary, a strong connection among the single dominant vortex, the recirculation bubble properties and Γ is evident. As will be clarified below, their complex flow behaviour is significant for the wall pressure statistics.

4.2.1 POD analysis

The classical POD method of the snapshot has been applied to characterize the dynamic of the vortex into the cavity of the RPE with square cavity. Such a method has been applied in two different domains, Ω_1 and Ω_2 , rendered with red and blue rectangles in Fig. 4.2.1. The spirit of the first analysis was to show that the form of the modes is affected by the domain size and the energy of the flow structures contained within, as was pointed out by Maurel et al. [2001]. These domains are centered in the vortex center and

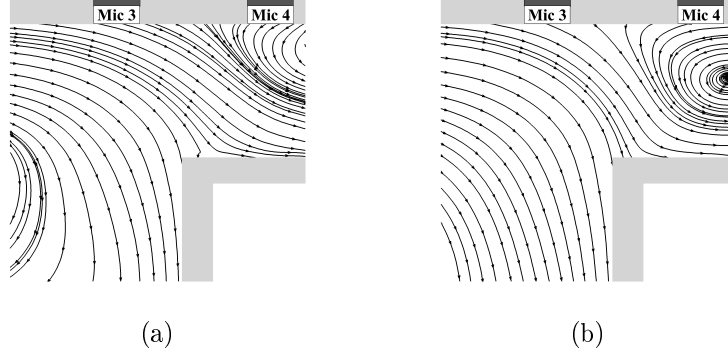


Figure 4.4: Streamlines of the averaged velocity field, corresponding to FOV_2 and measured at $Re = 50271$ for $\Gamma = 2.6$ (a), $\Gamma = 3.8$ (b).

they are small enough to exclude the jet by analysis. As a matter of fact, for the case under investigation, the fluctuating kinetic energy of the jet is much higher than the vortex energy. Further the vortex dynamic may be *covered* by the dynamic of the jet. For this reason Maurel et al. [2001] introduced the concept of extended POD based on an identification of different domains characterized by flow structures with a comparable fluctuating energy.

In order to avoid, the procedure of the selection of the domain with comparable fluctuating energy as in extended POD, a novel technique to recast the POD information is proposed. Such technique, formulated in the context of present work, is called POD_{lm} . The main advantages of POD_{lm} is its domain and fluctuating energy regardless. So a preliminary section of the different domain, as in extended POD is not needed. In addition by means of POD_{lm} the physical interpretation of the modes can be more simple than in the classical one.

The results provided by applying the POD in Ω_1 are reported in Fig. 4.6. Modes 1 and 2 exhibit a shape similar to those shown in Fig. 3.4 for the same analysis computed on the Rankine perturbed vortex. So the physical interpretation of the modes can be based on the previously experience on the data numerically simulated. In the experimental case, the first mode is characterized by a sizeable region of vectors with parallel direction as

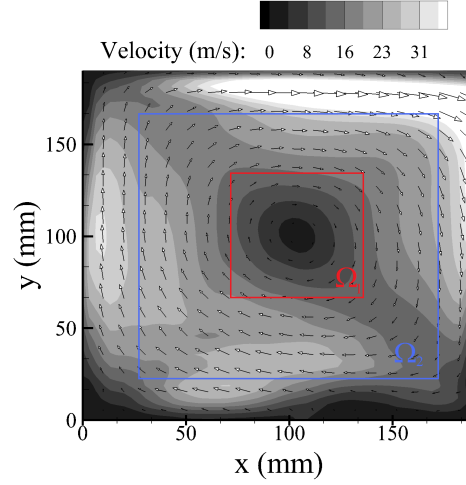


Figure 4.5: POD domain, evidenced by red and blue rectangle centered on the vortex core of the main scale formed in the cavity.

illustrated by Fig. 4.6 (b). As seen previously for the Rankine vortex, such a behaviour corresponds to the vortex core wandering. This implies that the vortex oscillates along a direction transversal with respect to the direction of the vectors. In addition, since this mode is the first, that is the most energetic, the vortex wandering is the dominant dynamic. With reference to Fig. 4.6 (c), the second mode is a deformation field with an angle $\gamma \cong \pi/4$. As known, a deformation field induces an expansion/contraction of the vortex along x/y -axis, in other words an asymmetric vortex flapping. Higher order modes, e.g. mode 3 and 4 (see Fig. 4.6 (d, e)), have an *energy* content lower than 5%, as can be seen by observing the eigenvalue spectrum in Fig. 4.6 (f), so they have not been taken into account in the present discussion.

Extending the analysis to domain $\Omega_2 > \Omega_1$, the physical interpretation of the first two modes appears less simple, as the mode shapes are more complicated indeed. In the first mode, reported in in Fig. 4.2.1 (a), a zero wave number disturbance is distinguishable. As discussed in chapter 3, this disturbance induces an isotropic flapping of the vortex. Since this disturbance exhibits the same rotating direction as the mean field, when the POD coefficient $a_1(t)$ assume positive sign, the vortex becomes expanded, whereas

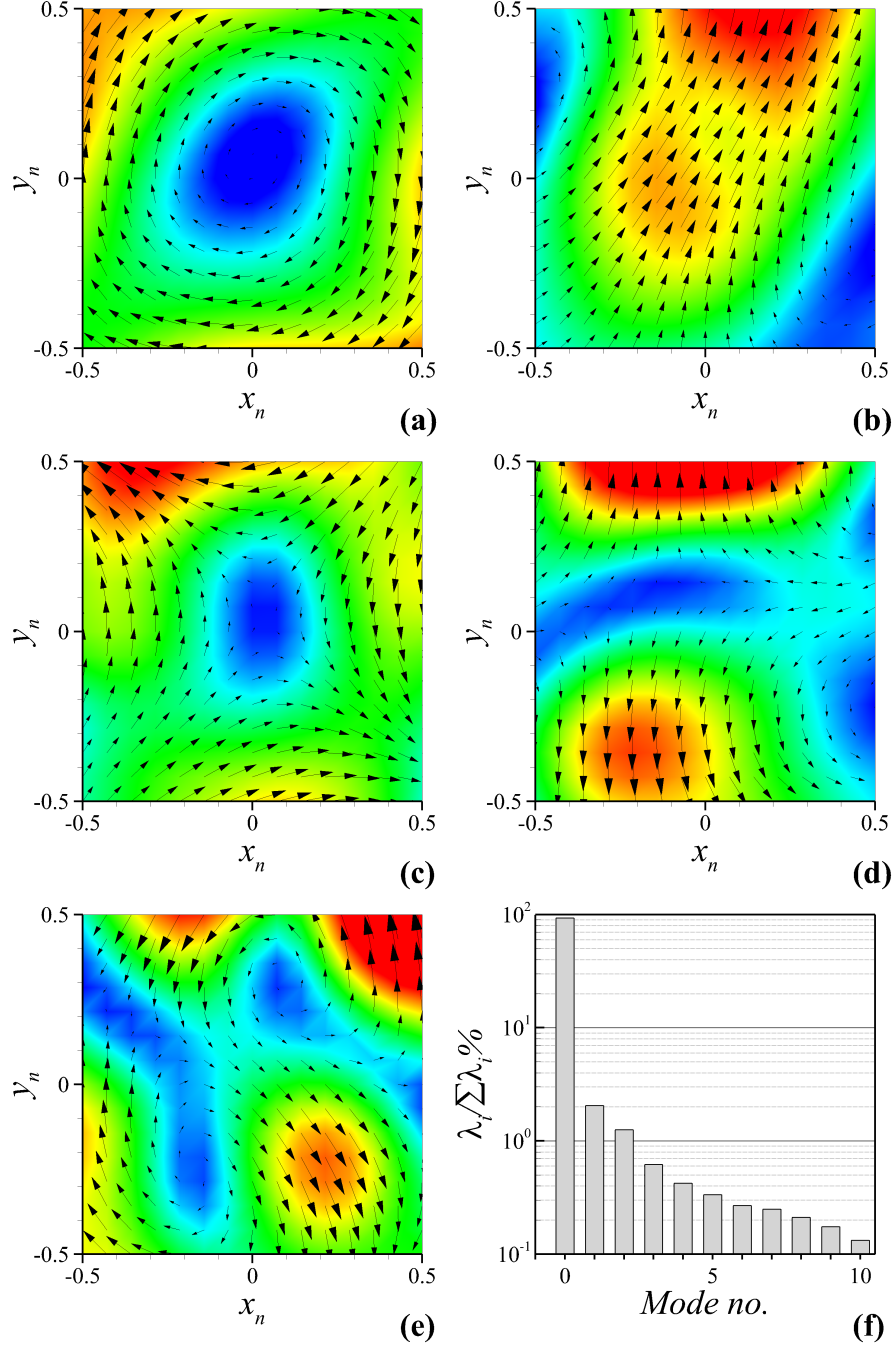


Figure 4.6: First four modes: 0 (a), 1(b), 2(c), 3(d), 4 (e) and eigenvalue spectrum obtained performing POD on Ω_1 domain (f).

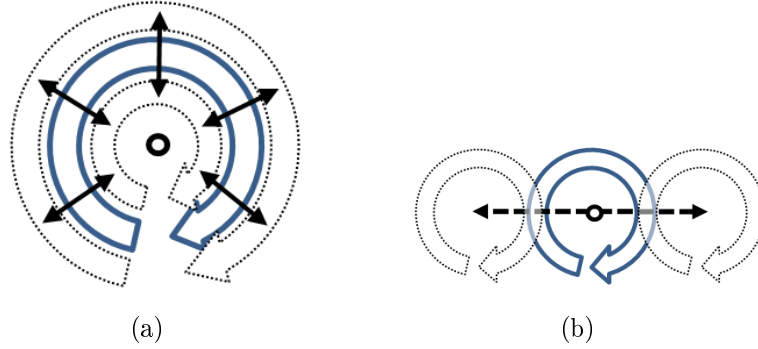


Figure 4.7: Sketch of the dominant dynamic identified: vortex flapping (a) and vortex wandering (b).

for $a_1(t) < 0$ a vortex contraction occurs, as sketched in Fig. 4.7(a).

With reference to the second mode (Fig.4.7(b)), a region with quasi-parallel vector is observed. As just discussed, this form of perturbation represents the vortex wandering dynamic. As a first-order description, it is easy to figure out that a combination of the mode 2 with the mean field leads to a displacement of the vortex perpendicular to the direction of the second mode, towards the upper-left corner of the Ω_2 domain. Any other analysis, extended to domains bigger than Ω_2 , are not herein reported since the physical interpretation of the modes is not clear. Indeed Maurel et al. [2001] et al., in a velocity field similar to that under investigation, have pointed out that POD is not helpful if one flow region of interest contains only a small percentage of the total kinetic energy. For this reason the concept of extended modes has been introduced by computing POD in both the flow domain and in sub-domains (Maurel et al. [2001]).

For the sake of clearly POD_{lm} are applied on a domain higher than Ω_2 where the jets are included. The limit cases and the mean field are reported in Fig. 4.9. The x -axis is normalized with the depth of the cavity, whereas the velocity is divided by a reference velocity. In Fig. 4.9 (a) the mean velocity profile, extracted at vortex center, and the limit cases referred to first mode are shown. It is noticeable the vortex expansion/contraction delimited by limit cases (red dashed line). Moreover any displacement of the vortex core

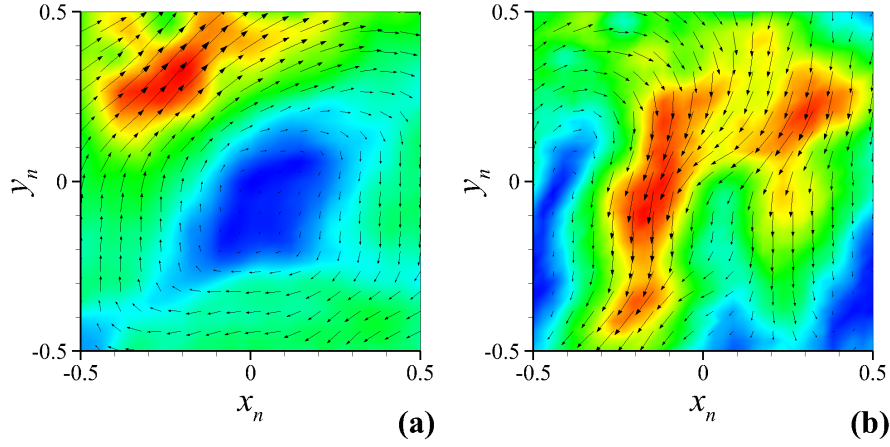


Figure 4.8: First two modes: mode 1(a) and mode 2(b) provided computing POD on Ω_2 domain.

does not occur. A similar consideration can be carried out by observing the iso-velocity lines in Fig. 4.9 (c) referred to the same data. In Fig. 4.9 (b) and (d) the velocity profile and iso-velocity line describe, comparing to the average field, a nearly rigid translation of the vortex core.

For different cavity aspect ratio the first two mode exhibit the same structures of the disturbance, describing the same vortex dynamic: vortex flapping and vortex wandering (see Fig. 4.10).

In Fig.4.11 are reported the energy associated to modes for different value of Γ . An expected behaviour occurs for $\Gamma = 3.2$ or $D = 160$ where the energy associated to first mode is higher, this result mean that the vortex flapping is more evident for this geometry, at same time a noticeable reduction of energy associated to vortex wandering is highlighted. Concluding the more unstable geometry from flapping dynamic point of view is identified.

4.3 Acoustic numerical simulation

A three-dimensional finite element model of RPEs, using the commercial software COMSOL, has been developed and directly solved in the frequency domain. The pressure distribution is provided over the frequency range 50-

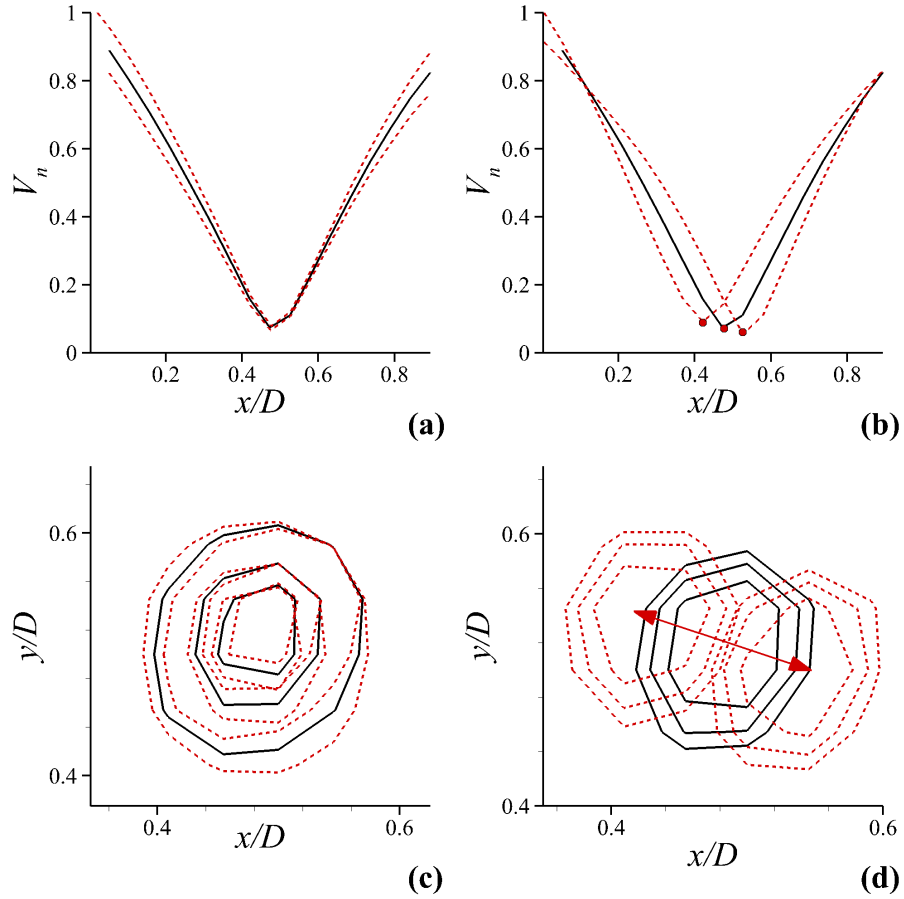
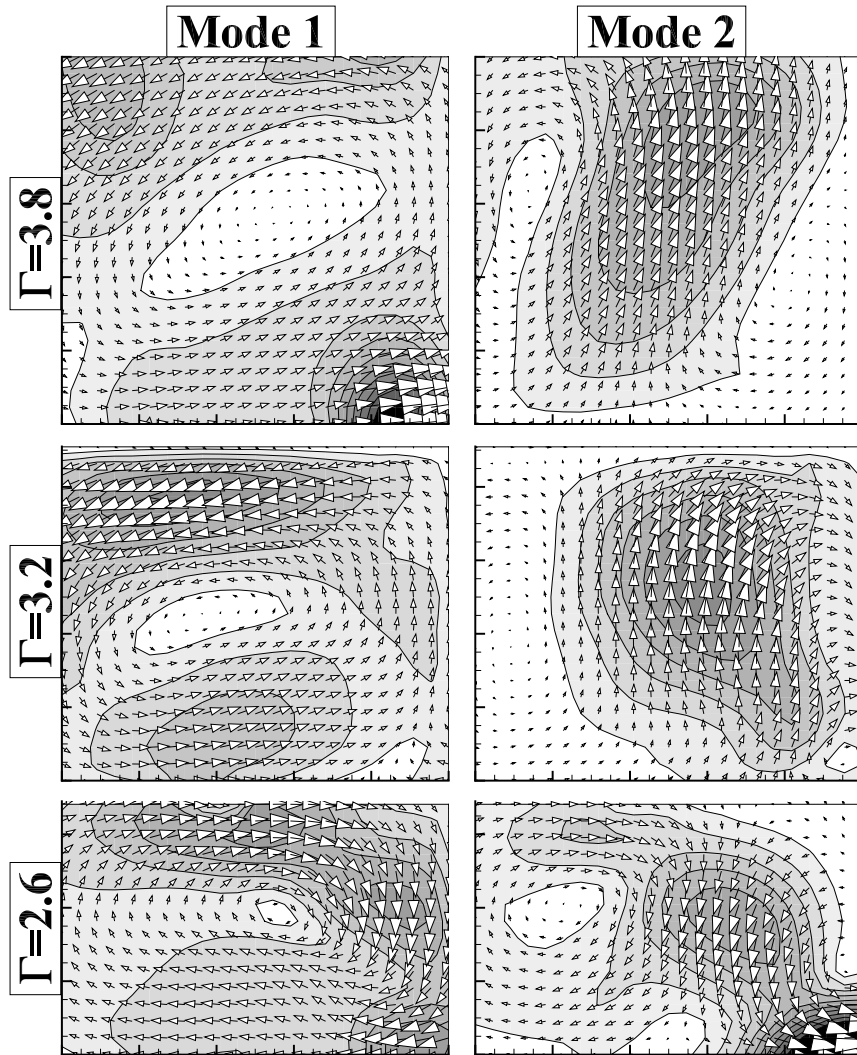
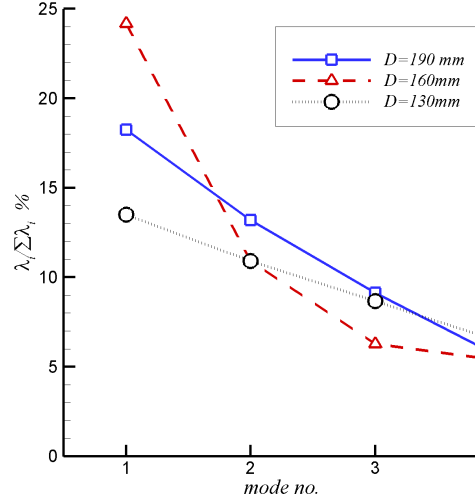


Figure 4.9: Average velocity (black solid line) and limit cases (red dashed line) profiles referred to the first mode(a). Average velocity (black solid line) and limit cases (red dashed line) profiles referred to the second mode (b). Average velocity (black solid line) and limit cases (red dashed line) iso-velocity line referred to the first mode(c). Average velocity (black solid line) and limit cases (red dashed line) iso-velocity line referred to the second mode(d).

Figure 4.10: First two modes for different Γ .

Figure 4.11: Eigenvalue spectrum varying Γ .

2000Hz with 1Hz increment. All sides of the exterior domain realized around the RPE has been modeled as open radiating into free space. A pressure fluctuation magnitude equal to 1Pa has been imposed on the vertical face of the exterior domain in front of the RPE outlet, as a forcing. Dissipative effects due to the viscous losses of the air moving back and forth in the neck, have been neglected in this model. The region of the exterior domain in close proximity to the RPE opening exhibits a non-planar sound field and a dependence over the mesh density. Hence a mesh refinement procedure has been applied, in order to achieve solutions independent by the mesh and in agreement with the experimental modal test. A scheme of the mesh adopted after the refinement is given in Fig. 4.12. This configuration corresponds to 10^5 tetrahedral cells. In order to take into account the effect of the orifice geometry, the wall thickness has been also modeled.

The first three modes achieved in the case of square and rectangular cavities are reported in Fig. 4.13 and Fig. 4.14 respectively. In both cases all the modes reported can be considered as a linear combination of longitudinal and transversal modes except in the case of the rectangular cavity where the second mode is split into longitudinal and transversal components. This

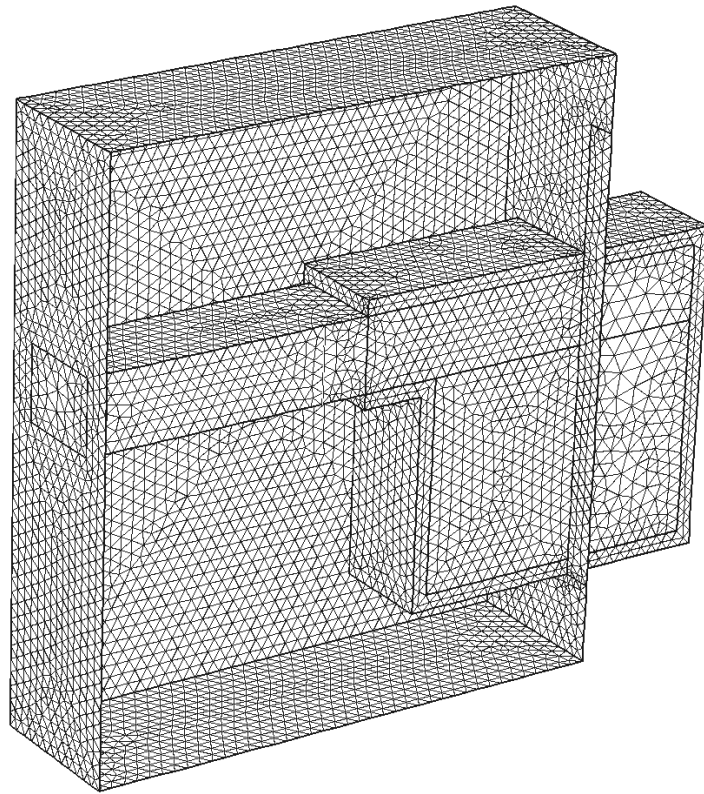


Figure 4.12: Sketch of the mesh realized.

Γ	1LT (Hz)	2LT	2L (Hz)	2T (Hz)	3LT (Hz)
3.8	185	936	/	/	1273
3.2	202	/	935	1083	1378
2.6	225	/	942	1321	1534

Table 4.1: First three mode frequencies varying Γ .

result seems to suggest that a model based on longitudinal propagation of the first mode, as usually adopted for classical combustors [Altay et al., 2009, 2010, Poinot and Veynante, 2005] is not appropriate for this kind of geometry.

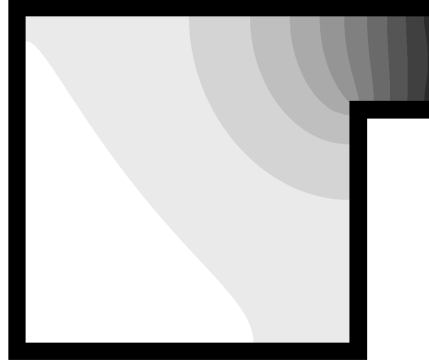
The numerically obtained FRF_{SPL} is reported in Fig. 4.15. When Γ raises, the frequency of the first mode decreases, whereas the intensity increases substantially. Furthermore the splitting of the second mode, indicated in Tab. 4.1. as 2LT, when the cavity becomes rectangular in the longitudinal 2L and transversal mode 2T is also observed. Finally, focusing our attention on the acoustic field in the exterior domain frequency of the first mode (185Hz) for the geometry with square cavity, shown in Fig. 4.16, it is noticeable that the mode it is developed in this region that suggesting the use of an end-correction to take into account this effect.

Finally, focusing our attention on the acoustic field into exterior domain at 185Hz (frequency of the first mode of the geometry with square cavity), shown in Fig. 4.16, it is noticeable that the first mode is developed also into exterior domain thus suggesting the use of an end-correction in the model.

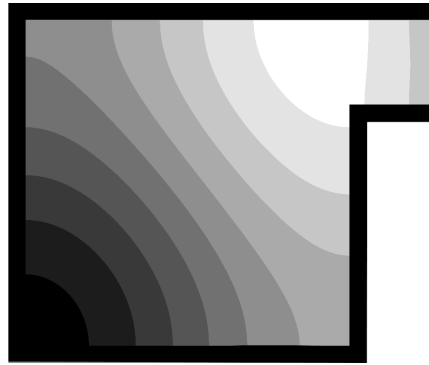
4.3.1 End-correction

The FRF_{SPL} obtained by means of the experimental modal test is shown in Fig. 4.17. In agreement with numerical simulation, the frequency and amplitude of the first mode is affected by Γ as described in §4.3.

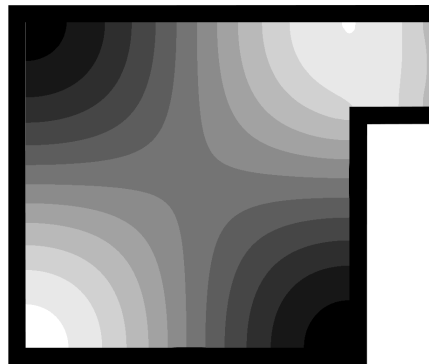
Although the geometry investigated is sufficiently different from a classical Helmholtz resonator. The first mode frequencies exhibit in log-log scale the typical $-1/2$ slope of the Helmholtz resonator. Furthermore a weak frequency drifting appears by varying the transversal length of the neck, as



(a)



(b)



(c)

Figure 4.13: First three modes occurring in the square RPE. Grey levels represent the SPL in an arbitrary scale.

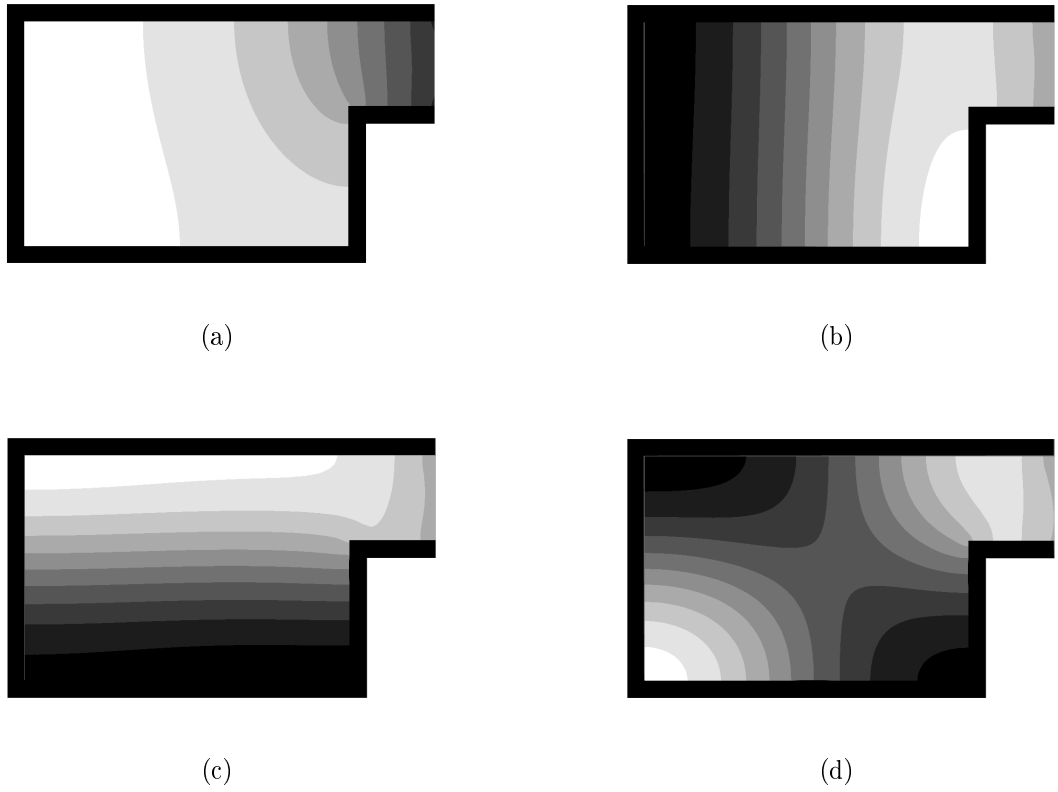


Figure 4.14: First three modes occurring in the rectangular RPE: (a) first mode, (b) second longitudinal mode, (c) second transversal mode and (d) third mode. Grey levels represent the SPL in an arbitrary scale.

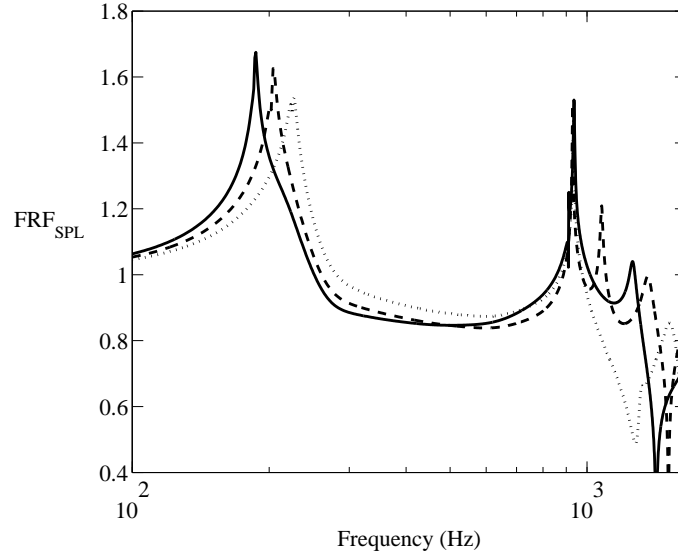


Figure 4.15: Frequency Response Function for the three different configurations: $\Gamma = 3.8$ (—) , $\Gamma = 3.2$ (---), $\Gamma = 2.6$ (·····).

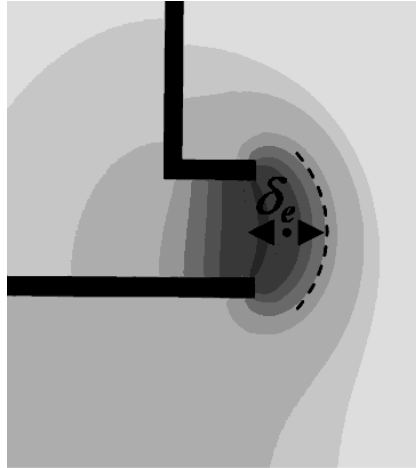


Figure 4.16: Enlargement of the exterior acoustic field simulated at the first mode frequency. The length of the exterior end correction δ_e is qualitatively estimated and superimposed on the figure. The grey levels represent the sound pressure level in arbitrary scale.

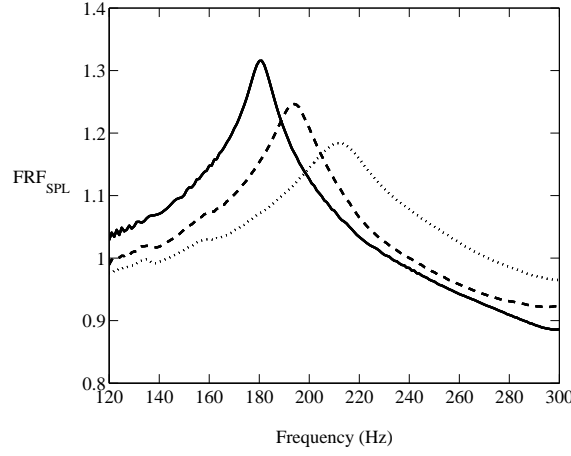


Figure 4.17: Frequency Response Function for three different configurations: $\Gamma = 3.8$ (—), $\Gamma = 3.2$ (---) and, $\Gamma = 2.6$ (·····).

reported in Fig. 4.18. This behaviour is due to the development of the first mode in the exterior domain as was shown in Fig. 4.16. For this reason a theoretical model based on open-end boundary condition does not predict correctly the first mode frequency. In order to improve the accuracy of the classical expression of HR:

$$f = \frac{c_0}{2\pi} \sqrt{\frac{1}{\Gamma L l}}, \quad (4.1)$$

the neck length is usually *corrected* by adding a so called end-correction term:

$$l' = l + \delta_e + \delta_i = l + 2\delta_R = l + \alpha \sqrt{\frac{dW}{\pi}}, \quad (4.2)$$

$$f = \frac{c_0}{2\pi} \sqrt{\frac{1}{\Gamma L l'}}, \quad (4.3)$$

where $\sqrt{Wd/\pi}$ is the hydraulic radius of the neck [Pierce, 1994, p.349]. The end-correction for axisymmetric HR, expressed in dimensionless form, depends on of the cavity-neck diameters ratio and it ranges between two well-known values, $0.785 < 2\delta_r/d < 0.848$ [see Selamet et al., 1997]. In the present case it has been checked that the most common end-correction

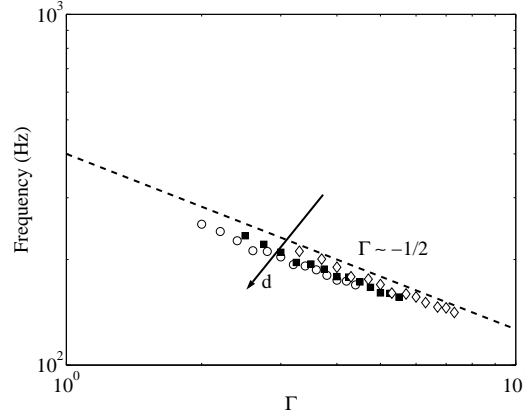


Figure 4.18: First mode frequency referred to $d = 50\text{mm}$ (\circ), $d = 40\text{mm}$ (\blacksquare), $d = 30\text{mm}$ (\diamond).

formulations do not lead to a good agreement with the experimental results, probably due to the length-width ratio of the geometry under investigation. Hence, a novel end-correction formula is proposed by a linear fitting of the experimental data in log-scale. Eventually an analytical expression of α is derived:

$$\alpha = \left[\frac{1}{L} \left(\frac{c}{2\pi 10^q} \right)^2 - l \right] \sqrt{\frac{\pi}{dW}}, \quad (4.4)$$

where q is the intercept of the linear fitting of the experimental data and its value is close to 2.549 for all cases under investigation. In Fig. 4.3.1 a comparison between frequencies experimentally provided and those calculated using Eq. 4.3 applying the end-correction here proposed (Eq. 4.4) is measured showing a good agreement. The bisector of the plot plane is superimposed to the data.

4.4 Wall pressure fluctuation statistics

The complex flow field depicted in this work (jet-wall interaction, a dominant macro-scale, separation bubble dynamics, adverse pressure gradient) is the counterpart of a complex aeroacoustic behaviour. The analysis of the wall pressure power spectra is first focused on the low frequency range, where the

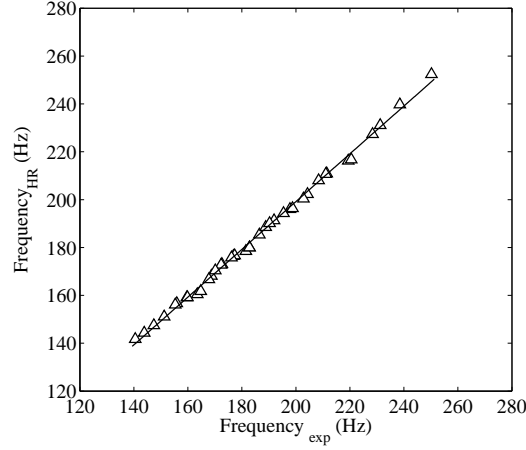


Figure 4.19: First mode experimental frequency versus frequency predict applying empirical-end correction. Linear fitting of the data is superimposed.

signature of the acoustic modes is relevant. In the spectra shown in Fig. 4.20(a) a dominant peak appears at about the same frequency as the first acoustic mode, in agreement with the acoustic numerical and experimental results. More specifically it is found that all geometries herein investigated follow a Helmholtz resonance scaling law. The solutions of Eqs.1.13, 1.16 and 1.17, including the end-correction, are also reported in Fig.??(b) to compare the experimental results with different formulas to predict the first mode frequency. The solid curve is the solution of the HR equation, whereas the dashed curve is the solution of eq. 1.13 based on the longitudinal model. The frequency of the dominant peak in the spectrum varying Γ is superimposed to the curves. The experimental data follow the HR scaling law demonstrating that for this kind of geometry a longitudinal model is not suitable to predict the first mode frequency.

$$f = \frac{c_0}{2\pi} \sqrt{\frac{1}{\Gamma L'}} \rightarrow f \propto \Gamma^{-1/2}, \quad (4.5)$$

The solution including the end correction proposed in §4.3.1, represented by the solid line in Fig. 4.20(b), is superimposed to the experimental data, showing a good agreement between the phenomenology and the theoretical

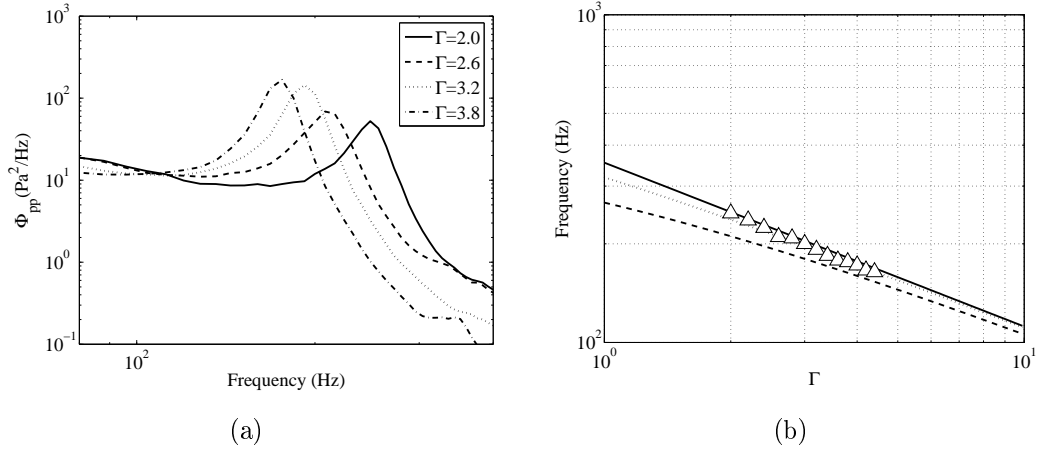


Figure 4.20: Power spectral density referred to microphone 5 obtained varying Γ and keeping Re constant (a). First mode frequency, provided by means aeroacoustic test (\triangle), superimposed to solutions of Eq. 1.17 (*cubical HR* —), Eq. 1.16 (*long cavity HR* · -) and Eq. 1.13 (*double duct* - - -) (b).

prediction proposed.

Taking into account the latter consideration, a reduced *Strouhal* number can be defined as follows:

$$St_{\Gamma} = \frac{f d_{in}}{U_{in}} \Gamma^{1/2}, \quad (4.6)$$

where U_{in} is the mean inlet velocity and d_{in} the inlet section diameter. Such a reduced *Strouhal* number form takes into account the variation of Γ and, as shown in Fig. 4.21, leads the spectra to collapse. The y-axis is normalized with respect to the inlet dynamic pressure (q_{in}) using the local reference time $\tau = d_{in}/U_{in}$. The data collapse is satisfactory except for $St_{\Gamma} > 0.5$ thus confirming the self-similar structure of the wall pressure fluctuations spectra. In addition, for normalized PSD, the effect of Re is reported in Fig. 4.21(b). As expected, a collapse of the peaks is no longer observed whereas the spectra collapse well in the high frequency range. In order to investigate the high frequency behaviour for $St_{\Gamma} > 0.5$ the PSD for $\Gamma = 2.6$ and $\Gamma = 3.8$ are computed at three different Re . The spectra are reported in Fig. 4.22(a) and Fig. 4.22(b).

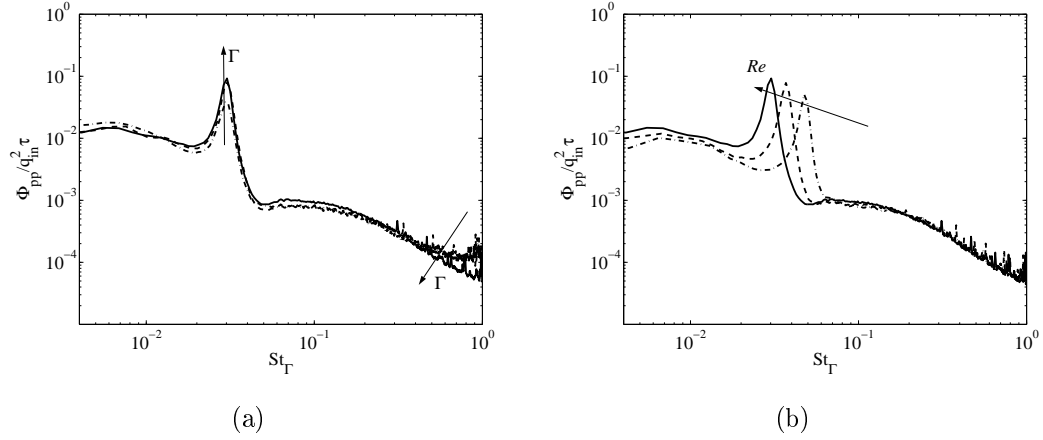


Figure 4.21: Power spectral density of the wall pressure referred to station 1, the pressure is normalized by q_{in}^2 . The data are taken at $Re=50271$ and $\Gamma = 2.0, 2.6, 3.2, 3.8$ (a). The data are computed at $Re=50271, 36865, 30163$ and $\Gamma = 3.8$ (b).

Two different power law decays, -1 and -2 , are observed at high frequency for the rectangular and the square cavity respectively. The power law is not dependent on Re , but it is related to the flow dynamic. The slope equal to -1 , measured for $\Gamma = 2.6$ is characteristic of equilibrium turbulent boundary layer (TBL), associated with turbulent activity in the log layer [see Bradshaw, 1967]. Whereas a power decay equal to -2 has been found in *non-equilibrium* TBL. Na and Moin [1998] performed a DNS of a TBL developing over a flat plate, under mild and strong imposed adverse pressure gradients (APG). In the latter case a power law decay with exponent close to -2 was observed for the spectra downstream of the reattachment point. With reference to Fig. 4.3 the APG at the location of the microphone 1 ($x/(L+l) = 0.46$) is higher for $\Gamma = 3.8$ than $\Gamma = 2.6$. For this reason the shear of vorticity near the wall, referred to the square cavity, appears thickened and more irregular than in the other case, as it is clear by comparing Fig. 4.22(f) and 4.22(e). This demonstrates a different activity of the vortical structures close to the wall.

In Fig. 4.22(c) the spectra associated to the transverse microphone (microphone 5) are reported for different aspect ratio. We focus our attention

only on two cases $\Gamma = 3.8$ and $\Gamma = 2.6$. In the first case the spectral slope computed assumed the value -4 and the vortex center is located at the same position of the microphone, as can be seen in Fig. 4.22(f)). The same power law decay, f^{-4} , has been found by Na and Moin [1998] in the separation bubble. In the second case for $\Gamma = 2.6$ vortex core appears displaced respect the position of the microphone 5, at the same time the slope is changed from f^{-4} to -2 . So the spectral decay variation can be ascribed to vortex core position.

The coherence time of an eddy is proportional to its scale and the larger eddies are convected at higher velocity, U_c [see Camussi et al., 2006]. So the convection velocity is an increasing function of the distance ξ between the sensors, as pointed out Brooks and Hodgson [1981]. Corcos [1964] defined an average convection velocity U_c based on the cross-spectral phase ϕ_{ij} between a couple of sensors, separated by distance ξ , as:

$$\phi_{ij} = \frac{\omega \xi}{U_c(\omega, \xi)}, \quad (4.7)$$

The U_c magnitude is directly dependent upon the nature of the pressure perturbations. Specifically, pseudo-sound pressure in TBL would be primarily driven by vortical structures advected by the mean flow close to the wall. Typically the pseudo-sound perturbations are expected to be characterized by convection velocity which is a fraction of the external inviscid mean velocity. On the other hand, an acoustic pressure perturbation propagates through space at the sound speed; thus, in an incompressible TBL, it moves at velocity much larger than U_c . In equilibrium boundary layers the hydrodynamic pressure is expected to be dominant as an effect of the turbulent structures advected close to the wall.

The cross-spectral magnitude and phase, for a square cavity, referred to microphones 1 and 2, is displayed in Fig. 4.4. The phase exhibits two trends, a *plateau* at low frequency and a region with negative slope at high frequency. The first one ranges from $10Hz$ up to the frequency of the first acoustic mode, the second one ranges from the first mode frequency up to $2000Hz$. The plateau is ascribed to acoustic effects since all pressure time

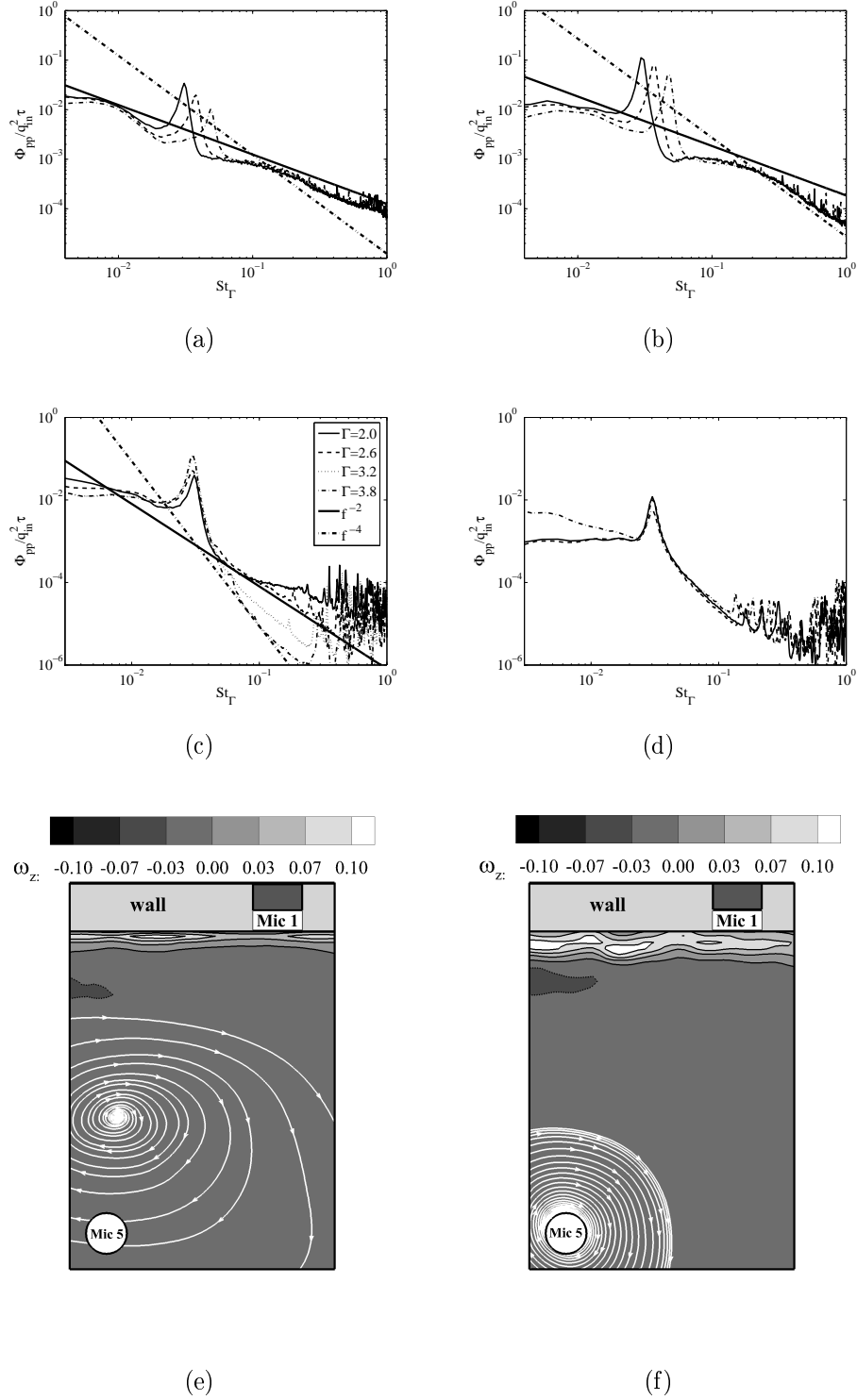


Figure 4.22: Normalized power spectral density referred to microphone 1 for $Re = 50271$ (—), $Re = 36865$ (---) and $Re = 30163$ (· -) and $\Gamma = 2.6$ (a) and $\Gamma = 3.68$ (b). Normalized power spectral densities referred to microphone 5 computed for different Γ , $Re = 50271$ (c). Normalized PSD computed at $Re = 50271$ and different cavity aspect ratio: $\Gamma = 3.8$ (—), $\Gamma = 3.2$ (---) and $\Gamma = 2.6$ (· -) (d). Averaged vorticity field (contour) and streamlines (white lines) obtained at $Re = 50271$ for two values of cavity aspect ratio: $\Gamma = 2.6$ (e) and $\Gamma = 3.8$ (f).

scale propagates at the same velocity. On the other hand, the negative slope, with reference of eq. 4.7, is a consequence of convective effects. This interpretation is also confirmed using a procedure for analysing the cross-correlations between microphone 1 and 2. In particular two signals is derived by each raw signal applying different frequency filters:

- low-pass filtered signal (LPFS) with cutoff frequency equal to first acoustic mode frequency,
- high-pass filtered signal (HPFS) with cuton frequency equal to first acoustic mode frequency.

then the couples of signals, referred to microphone 1 and 2, filtered applying the same algorithm have been cross-correlated. Eliminating the contribution of the highest harmonic component the information embedded in the pressure fluctuations, otherwise covered by the amplitude of the first acoustic mode, can be highlighted by the cross-correlation. In Fig. 4.24(a) and 4.24(b) the cross-correlations of the LPFSs and HPFSs are respectively displayed for different inlet velocity. For LPFSs the time delays, have low negative values, regardless of the velocity inlet. Therefore the phenomenon, identified with low-pass filter propagates with high velocity in opposite direction of the flow, so can be ascribed to acoustic waves. For HPFSs the time delays obtained is positive, affected by velocity inlet and propagates at velocity with the same order of the velocity inlet, so the pressure fluctuations at high frequency is convected by the mean flow. The calculated convective-inlet velocity ratio of the HPFSs are listed in Table 4.2. These values are close to 0.5 and are not affected by Γ and Re for all the examined configurations, that indicates a fluid dynamic convection of the pressure fluctuation for frequency higher than the first mode frequency in according with the considerations referred to Fig. 4.4. In conclusion, we can consider the first mode frequency as a boundary between two frequency regions: low frequencies where all pressure fluctuations are ascribed to acoustic and high frequencies where all pressure fluctuations are due to convection effects, moreover that phenomenologies propagating in opposite directions.

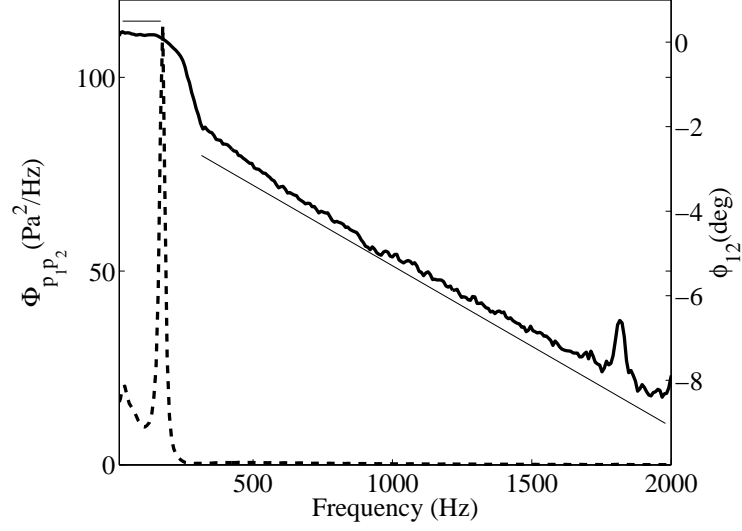


Figure 4.23: Magnitude (— — —) and phase (—) of the cross-spectrum referred to microphones 1 and 2 computed for the square cavity at $Re = 50271$.

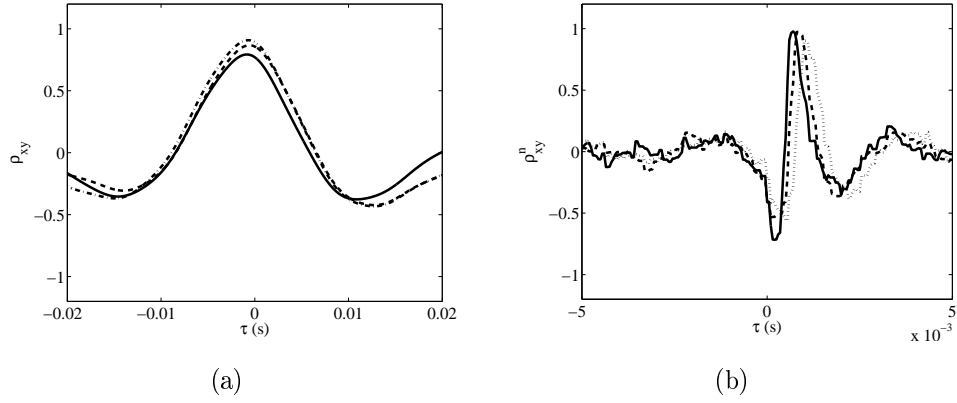


Figure 4.24: Cross-correlation between microphone 1 and 2 computed after filtering the raw signal with low-pass filter (a) and high-pass filter (b). The curves are provided for three different Re numbers: 50271 (—), 36865 (— —) and 30163 (· · ·).

Γ	Re	U_c	U_c/U_{in}
3.8	30163	23.6	0.48
3.8	36865	29.1	0.46
3.8	50271	37.7	0.49
2.6	30163	24.8	0.50
2.6	36865	32.9	0.52
2.6	50271	38.0	0.49

Table 4.2: The convention velocities and convection-inlet velocity ratios for square and rectangular cavities and different Re numbers.

The overall amplitude of the pressure fluctuations have been characterized through the computation of the root mean square pressure coefficient Cp_{rms} , defined as follows:

$$Cp_{rms} = \frac{\sigma_p}{\frac{1}{2}\rho U_{in}^2}, \quad (4.8)$$

where σ_p represents the standard deviation of the pressure signal and ρ is the fluid density. The values assumed by Cp_{rms} , as a function of Γ , are reported in Fig. 4.25 for all microphone locations. In the region upstream of the neck the largest pressure levels are measured (microphones 1, 2 and 3), whereas an important reduction of Cp_{rms} occurs in the neck (microphone 4). A quite similar behaviour occurs for each Re investigated. The relevant reduction of Cp_{rms} is ascribed to the partial reflection of acoustic waves due to the section discontinuity that leads to a reduction of the acoustic energy transmitted from the cavity to the neck. Furthermore we observe that the pressure fluctuation acquired by microphone 4 is more dispersed than for the other microphones, since when Γ is 2.6 a considerable increase of the Cp_{rms} occurs in the neck and, as displayed in Fig. 4.22(d), a significant increase of the energy at low frequency is also observed.

In order to clarify this aspect, the probability density functions, PDFs, of the wall pressure fluctuations have been computed for all microphone locations and for different Re . The random variable is represented in its reduced form in order to have zero mean and unitary standard deviation. The PDF shapes is weakly dependent on the microphone location, except

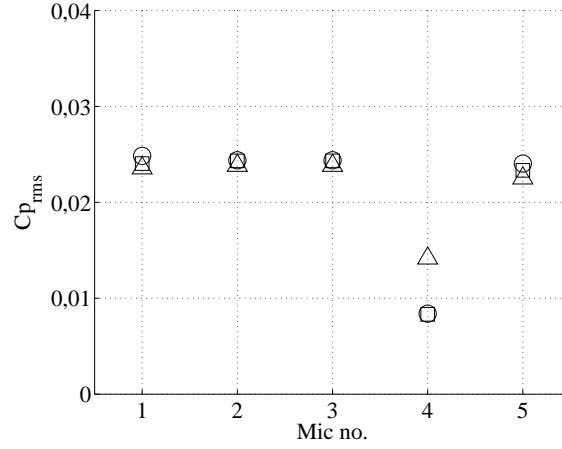


Figure 4.25: Cp_{rms} referred to all microphones computed for $Re= 50271$ and different Γ : $\Gamma = 3.8$ (\square), $\Gamma = 3.2$ (\circ) and $\Gamma = 2.6$ (\triangle).

for microphone 4, where a departure from the reference Gaussian curve is visible. More specifically the PDF referred to microphone 4 and $\Gamma = 2.6$ is positive skewed ($Skeewness = 1.01$ for $\Gamma = 2.6$ and $Skeewness = 0.06$ for $\Gamma = 3.8$). The origin of a such behaviour can be ascribed to the effect of the dynamics of the recirculation bubble as highlighted by the POD results. In the eigenvalue spectra, reported in Fig. 4.27, we can see that the energy associated to the first mode is for both cases an important part of the total fluctuating kinetic energy. As a consequence we can consider the first mode as strongly dominant over the others and focus our attention only on it. In Fig. 4.28 the first mode for different Γ is reported. In all cases a considerable bump marked by a red region, is identified. Despite this similarity, the mode shape exhibits a dependence on Γ evolving from about a *parallel vector* for $\Gamma = 3.8$ to an *asymmetrical vortical structure* for $\Gamma = 2.6$. In the latter case the higher intensity of the bump is close to the wall, above the microphone 4 location, and its shape denotes a dynamic of the recirculation bubble. It is therefore argued that the increase of Cp_{rms} and the wall pressure fluctuations at low frequencies is due to the recirculation bubble dynamic.

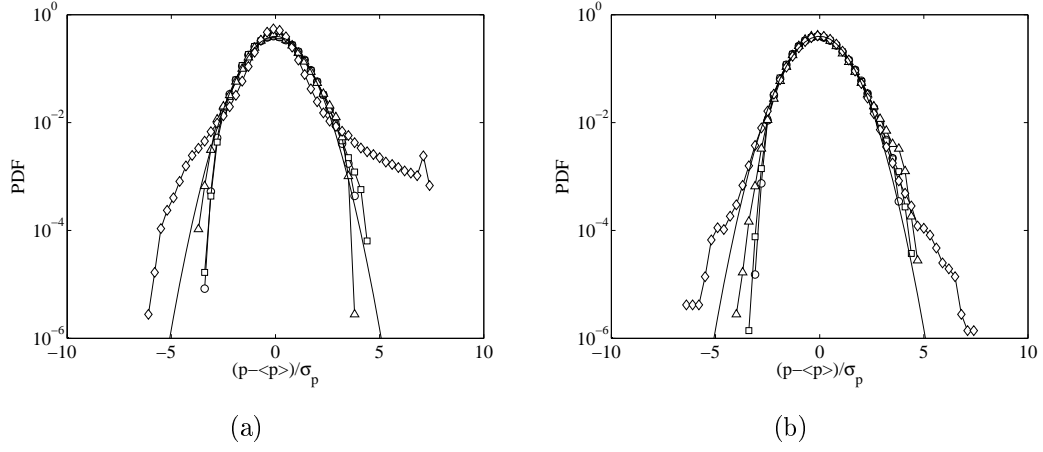


Figure 4.26: PDF of the wall pressure fluctuations reported in reduced variables. Different kind of markers correspond to different microphones: microphone 1(\circ), microphone 2 (\square), microphone 3 (\triangle) and microphone 4 (\diamond); PDFs in (a) are computed at $\Gamma = 2.6$, PDFs in (b) are computed at $\Gamma = 3.8$ and compared with normal distribution (—).

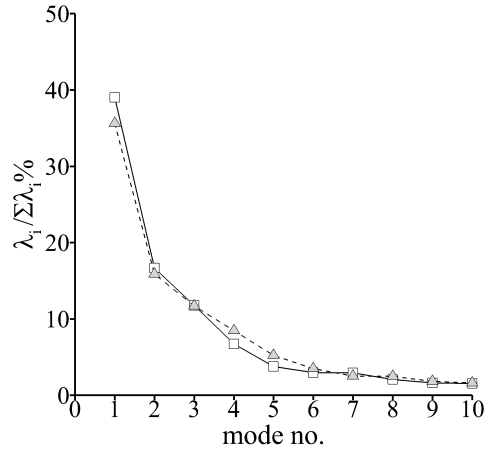


Figure 4.27: Spectrum of the eigenvalues referred to $\Gamma = 2.6$ (\square) and $\Gamma = 3.8$ (\triangle).

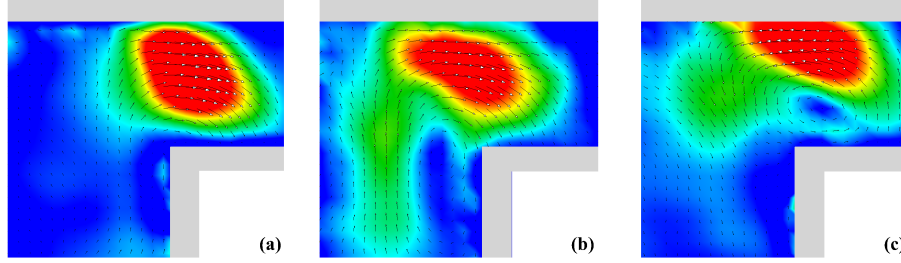


Figure 4.28: First mode of the proper orthogonal decomposition obtained varying Γ from 3.8 (a) to 2.6 (c) (left to right).

4.5 Concluding Remarks

The RPE aeroacoustic has been studied by applying several experimental techniques and through an acoustic numerical simulation. The fluid dynamic field for different geometrical configurations has been characterized. A very intense vortex is formed in the square cavity for $\Gamma \simeq 3.8$, suggesting this as an optimal geometry for designing a trapped vortex combustor with high performance in term of mixing dynamic.

In the experimental investigation herein described four experiments have been planned. PIV, microphones, array of pressure taps, loudspeaker have been employed to characterize the acoustic, aeroacoustic and fluid dynamic behaviour of the RPE. The experimental hardware e.g laser, synchronizer, CCD camera, microphones, flow-meters have been monitored using home-made software specifically implemented in Labview. Moreover specific softwares have been implemented in MATLAB to computing spectral, statistical, while POD analysis has been performed implementing a Labview software. As result, from the acoustic viewpoint, it has been shown that the RPE behaves like a Helmholtz Resonator, even though its geometry is very different from classical HR. In particular the frequency of the first mode scales with $\Gamma^{-1/2}$. Further in order to improve the accuracy of the first mode frequency prediction a novel end-correction has been derived. This end-correction demonstrates to be suitable for several geometry types: from square cavity ($\Gamma = 3.8$) to *short channel with small contraction* ($\Gamma = 2$).

Concluding the acoustic analysis has been shown that the classical model based on longitudinal propagation ($\tan(kL)\tan(kl) = \Gamma$), commonly applied to predict the first acoustic mode of the combustor chamber, is not adapted to predict the frequency of the first mode for this kind of geometry, sometimes adopted for realizing the trapped vortex combustor, while a model based on HR formulation has been demonstrated to be more accurate. The first acoustic mode also occurs in the aeroacoustic spectra as dominant tonal component. This tonal noise confirms that RPEs are affected by self-excited oscillations and that its application to realize combustion chamber can generate thermoacoustic phenomena. As a consequence, also in reactive condition, even though the small power associated to combustor reported in Fig. 1. A considerable tonal noise is radiated in stable condition.

The flow dynamic characterization has evidenced the formation in the cavity of a single vortex in solid rotation for all geometry considered. The vortex tangential velocity is generally more intense in the case of the square cavity decreasing with Γ . The POD analysis, in particular the novel method developed called POD_{lm} , has been highlighted that the dynamic of the vortex are the vortex flapping and wandering.

In the aeroacoustic spectra the high frequency region is affected by the APG that influence the jet-wall interaction inducing a non-equilibrium condition of the flow close to the wall and changing the high frequency spectra slope, from -1 to -2 . Finally, the recirculation bubble formed into the neck exhibits a dynamic depending by Γ that induces an increasing of the pressure fluctuations at low frequencies. Finally a reduced form of *Strouhal* number has been proposed by authors, obtaining a well collapsing of the wall pressure fluctuations spectra in an *universal* distribution. In the present thesis have proposed an aeroacoustic overview of rectangular partial enclosures, clarifying the nature of the peaks and the slopes occurring in the spectra and a theoretical model to predict the frequency of the first mode.

This research has been supported by ENEA, through a grant provided by Ministero dello Sviluppo Economico - Ricerca di Sistema Elettrico. The authors wish to thank ENEA represented by Eng. S. Giammartini for his supports of this activity.

Appendix A

Appendix

A.1 Particle Image Velocimetry

A.1.1 25 years of Particle Image Velocimetry

The initial groundwork for a PIV theory was provided by Adrian [1984] who described the expectation value of the auto-correlation function for a double-exposure continuous PIV image. This description provided the framework for the experimental design of this technique [Keane and Adrian, 1990]. Later, the theory was generalized to include multiple-exposure recordings [Keane and Adrian, 1991] and cross-correlation analysis [?]. The theory provided a description for the analysis of highly resolved PIV photographs, which was the common mode for a considerable time. However, nowadays PIV uses a charge-coupled device (CCD) cameras for direct recording of the particle images [?]. Despite the resolution and image format of CCD cameras are several orders of magnitude lower than that of a photographic medium, CCDs are more suitable for research purposes. The theory was further extended to include digital PIV images using the estimation of the displacement at sub-pixel level.

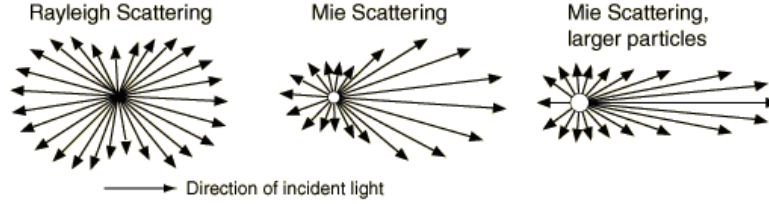


Figure A.1: Sketch of the scattering behaviour upon particles size.

A.1.2 Introduction

Particle image velocimetry (PIV) is a technique which enables instantaneous measurement of the flow velocity at several positions in a plane. The working principle is quite simple: the flow is seeded with light reflecting particles; usually smoke is used in air. The particles, used to seed the flow, should be small enough to follow the flow, but large enough to reflect the required amount of light and have an high directivity in the scattering signal.

In general PIV needs a high seeding density. A light sheet illuminates the particles in the measurement plane. Commonly a pulsed Nd:YAG laser (Neodymium Yttrium Aluminum Garnet) is used as the light source because of its high light intensity. The laser pulses have a duration time of $5 - 10ns$ and the energy in one pulse can be up to $400mJ$. The light beam coming out from the laser has an axisymmetric shape and passes through a cylindrical lens in order to form a planar light sheet. A camera is used to take two exposures of the illuminated plane. The two exposures should be taken within a short interval, so that the same particles are caught in both exposures. The two exposures can be taken either as a double exposure of one image or as two different images using a camera. The sensitivity of camera sensor such as a CCD-camera is measured in QE (quantum efficiency) which is the average number of electrons that are released from the sensor when it is hit by a photon. The QE is often wavelength dependent with a maximum efficiency in the blue-green part of the visible spectrum. The most sensitive cameras on the market today have Peltzier cooled (to reduce thermal noise) CCD-

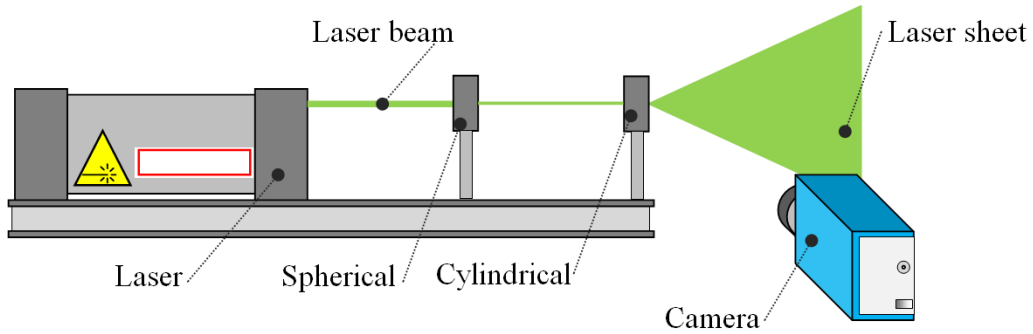


Figure A.2: Sketch of the PIV experimental set-up.

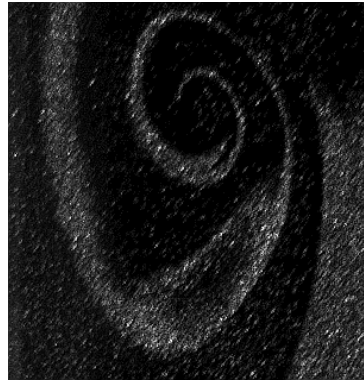


Figure A.3: Mie scattering image of a rolled-up reactive jet.

sensors. A sketch of the PIV experimental set-up is illustrated in Fig. A.1.2

An example of the result obtained by means of this technique is reported in Fig. A.1.2.

The method based on two images and cross-correlation is more commonly used and it will be treated in the remaining part of this chapter. A good reference book which deals with most of the PIV aspects is *Particle Image Velocimetry, practical guide* [Raffel et al., 1998].

A.1.3 Cross-correlation of images

The aim of the cross-correlation is to evaluate the distance that the particle pattern has covered during the inter-image time, Δt , and to convert this

into a velocity measure, \mathbf{u} . The relation between velocities and particle displacements, \mathbf{d} , is:

$$\mathbf{u} = \frac{\mathbf{d}}{\Delta t}, \quad (\text{A.1})$$

The cross-correlation function is calculated between smaller regions of images called interrogation areas (IAs). One can see a cross-correlation as a way to find the best match between two IAs obtained displacing the first IA on the second one. Clearly the required displacement results to be proportional to the average velocity of the particles within the IAs. Cross-correlation functions, denoted herein as $R_{AB}(x, y)$, where $A(x, y)$ and $B(x, y)$ denote a couple of images, can be calculated in a number of different ways. The direct method becomes very heavy to apply when huge data-sets have to be analysed. A more efficient way to estimate cross-correlation functions is by use of the fast Fourier transforms (FFTs). This method sensitively reduces the computation time switching from $O[N^4]$ to $O[N^2 \log_2 N]$ operations. When Fourier transforms are used, one can take advantage of the correlation theorem which states that the cross-correlation of two functions is equivalent to the product of their Fourier transforms, as follows:

$$R_{AB} \iff \hat{A} \cdot \hat{B}^* \quad (\text{A.2})$$

where \hat{A} and \hat{B} are the Fourier transforms of A and B , respectively and \hat{B}^* represents the complex conjugate of \hat{B} . Implicitly the use of FFTs corresponds to treat data as periodic. The periodicity can give rise to aliasing if the particles have moved a distance larger than half the size of the IA. A possible solution for aliasing problems is increasing the IA size or reducing the inter-image time Δt . Maybe a more serious problem concerning the FFTs is the presence of bias errors due to the finite size of the IAs. Such a bias leads to an underestimation of the peak magnitude for all displacements. A good strategy to avoid this problem can be to compute the convolution between the cross-correlation function and a weight function. A proper weight function can be equal to one for all points embedded into the image and zero elsewhere (*zero-padding*). Then the bias is removed by dividing the

correlation function by the weight function so defined.

A.1.4 Peak detection and subpixel interpolation

When the cross-correlation has been performed, a measure of the displacement is found by detecting the position of the highest correlation peak. Peak localization is possible with an uncertainty of $\pm 1/2$ pixel. However, the accuracy can be substantially increased by cross-correlation fitting and interpolation. The most common way to perform the interpolation using a three-point estimator. When the maximum correlation peak has been detected at (i, j) , the neighbouring values are fitted. In the case of a Gaussian peak fit, when the peak is assumed to have the shape $f(x) = C \exp[-(x_0 - x)^2/k]$, the displacements (x_0, y_0) can be described by:

$$\begin{aligned} x_0 &= i + \frac{\ln R_{i-1,j} - \ln R_{i+1,j}}{2 \ln R_{i-1,j} - 4 \ln R_{i,j} + 2 \ln R_{i+1,j}} \\ y_0 &= j + \frac{\ln R_{i,j-1} - \ln R_{i,j+1}}{2 \ln R_{i,j-1} - 4 \ln R_{i,j} + 2 \ln R_{i,j+1}} \end{aligned} \quad (\text{A.3})$$

Further interpolations can be performed at a subpixel level. In this case, parabolic fit of the peak and peak detection based on centroid algorithm are frequently used.

A.2 Acoustic simulation

A.2.1 Introduction to finite element methods

Finite element method (FEM) have been an active research area for nearly 40 years. In this work FEM for acoustics simulation has been applied on the reduced form of acoustic wave equation:

$$\frac{\partial^2 p}{\partial t^2} - c^2 \nabla^2 p = 0 \quad (\text{A.4})$$

where p is the pressure fluctuation and c the speed of sound. Eq. A.4, defined in the frequency domain, is well-known as *Helmholtz equation* and it is written as follows:

$$\nabla^2 \tilde{p} + k^2 \tilde{p} = 0 \quad (\text{A.5})$$

In Eq. A.5 k denotes the wave number and \tilde{p} the complex form of the pressure fluctuation.

In FEM method the acoustic domain is discretized in 3D element. The minimum size of the element, h , is mainly evaluated using maximum frequency criterion:

$$\begin{cases} h = \frac{c}{N f_{max}} \text{ for low frequencies} \\ h = \frac{c}{N f_{max} \sqrt{k}} \text{ for high frequencies} \end{cases} \quad (\text{A.6})$$

Typically the N coefficient assumes values from 6 to 10. The discretization of the domain reduces the Helmholtz partial differential equation A.5 in a linear algebraic problem:

$$\tilde{A} \mathbf{X} = \mathbf{B}, \quad (\text{A.7})$$

where \tilde{A} is the matrix of the coefficients, \mathbf{X} the variable vector and \mathbf{B} the constant vector. The inverse matrix of acoustic system, \tilde{A}^{-1} , can be found by its factorization in lower and upper triangular matrices:

$$\tilde{L} \tilde{U} \mathbf{x} = \mathbf{b} \Rightarrow \mathbf{x} = \tilde{L}^{-1} \tilde{U}^{-1} \mathbf{b}, \quad (\text{A.8})$$

where the lower and upper triangular matrices are denoted by \tilde{L} and \tilde{U} respectively, whereas \mathbf{x} and \mathbf{b} are the new variable and constant vectors of the system.

Typically, direct computation of a solution of the system requires a lot of memory. The multi frontal massively parallel sparse direct solver (MUMPS) splits the factorization operations in non-sparse frontal matrices in order to solve the system using an iterative algorithm. Newest iterative solver usually work in a Krylov subspace. It creates a Krylov subspace vectors and allows to find the coefficients able to obtain the minimum error when entering x_k as trial solution:

$$\begin{cases} x_k = \sum_{n=1}^k \alpha_n A^{n-1} \\ \min \|\tilde{A}x_k - b\| \end{cases} \quad (\text{A.9})$$

This approach requires less memory compared to direct methods. Since in the present work the test case is small and the wavelength of the mode under investigation is relatively big, the direct method is selected to realize the acoustic numerical model of RPE.

A.2.2 Boundary conditions

Initial applications of FEMs for time-harmonic acoustics have focused on interior problems with complex geometries for calculating the acoustic frequency response of enclosures or waveguides. In recent years, significant progress in the development of improved FEMs for acoustics, including exterior problems in unbounded domains, have been achieved. The problem here under investigation is a *hybrid* problem, as the studied geometry is a partial enclosure simulated in stand-alone configuration. So the domain under investigation can be divided into two regions: the first one is bounded by the interior of partial enclosure and its outlet section, while the second is an exterior domain where the forcing source is located, as rendered in Fig. A.4.

For this reason a particular attention has been given the boundary condition that models an unbounded domain (exterior domain). This exterior acoustics problem in unbounded domains presents a special challenge for FEMs. In order to use the FEM for exterior problems, the unbounded domain is usually truncated by an artificial boundary yielding a bounded computational domain. Reducing the size of the bounded domain the computation cost decreases, but it must be balanced by the ability to minimize any spurious wave reflection with a computationally efficient and geometrically flexible truncation boundary treatment. Recent numerical treatments including no-reflecting or absorbing layers conditions have been proposed. The criterion of choice depends on the shape and complexity of the geometry under investigation, inhomogeneities, frequency range, and resolution requirements, among other parameters.

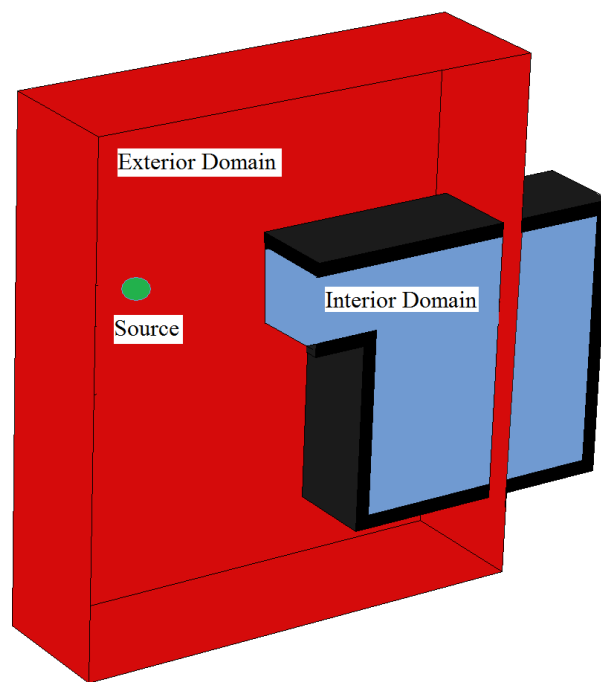


Figure A.4: Sketch of the domain where the acoustic response has been modeled.

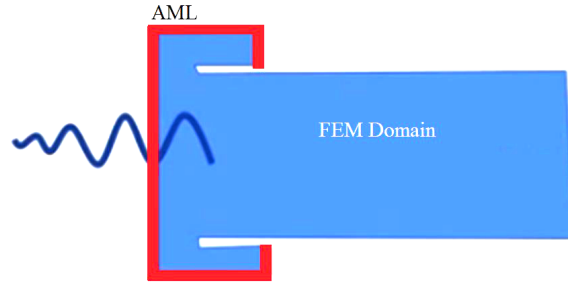


Figure A.5: Sketch of the wave propagation into a free-field outside a open-duct.

In FEM model a special treatment has been applied at outer FEM boundary, in order to satisfy *no-reflecting condition* (or *Sommerfield radiation condition*). For modeling the radiation condition with FEM, a large external domain is needed, although the matrix associated to this model is sparse and too large to obtain a suitable solving time. Therefore perfectly or automatically matched layer (PML/AML) is used to solve this problem. PML/AML is the non reflecting boundary condition applied in FEM that allows to handle the exterior radiation problems very efficiently. Significantly small FEM radiation models have been provided as the PML/AML domain has been built close to the actual physical FEM domain. Thereby the amount of necessary elements can be substantially reduced. A conceptual sketch of PML is rendered in Fig. A.5.

PML domain absorbs all energy and hence simulates radiating boundary conditions. PML shows a lower frequency limit below that the traveling wave are not absorbed. This condition is very useful for modeling the open-end duct behavior, as done in the present investigation.

A.3 Introduction to Labview

LabVIEW (short for Laboratory Virtual Instrumentation Engineering Workbench) is a system design platform and development environment for a visual programming language by National Instruments. The graphical language is

named "G" (not to be confused with G-code). Originally released for the Apple Macintosh in 1986, LabVIEW is commonly used for data acquisition, instrument control and industrial automation on a variety of platforms. The programming language used in LabVIEW, also referred to as G, is a dataflow programming language. Execution is determined by the structure of a graphical block diagram on which the programmer connects different function-nodes by drawing wires. These wires propagate variables and any node can execute as soon as all its input data become available. Since this might be the case for multiple nodes simultaneously, G is inherently capable of parallel execution. LabVIEW allows the creation of user interfaces (called front panels FP) into the development cycle. LabVIEW programs/subroutines are called virtual instruments (VIs). Each VI has three components: a block diagram, a front panel and a connector panel. The last is used to represent the VI in the block diagrams. Controls and indicators on the front panel allow an operator to input data into or extract data from a running virtual instrument. However, the front panel can also serve as a programmatic interface. Thus a virtual instrument can either be run as a program, with the front panel serving as a user interface, or, when dropped as a node onto the block diagram, the front panel defines the inputs and outputs for the given node through the connector panel. This implies each VI can be easily tested before being embedded as a subroutine into a larger program. The graphical approach also allows non-programmers to build programs by dragging and dropping virtual representations of lab equipment with which they are already familiar. The LabVIEW programming environment, with the included examples and documentation, makes it simple to create small applications. This is a benefit on one side, but there is also a certain danger of underestimating the expertise needed for high-quality G programming. The image above is an illustration of a simple LabVIEW program showing the dataflow source code in the form of the block diagram in the lower left frame and the input and output variables as graphical objects in the upper right frame. The two are the essential components of a LabVIEW program referred to as a VI.

A.4 Implemented softwares

Labview has been used to compute essentially three applications: the first one was devoted to manage the laboratory hardware, the second one to data post processing applying a POD algorithm, whereas the third simulated the perturbed dynamic of a Rankine vortex .

A.4.1 SYNCHRO

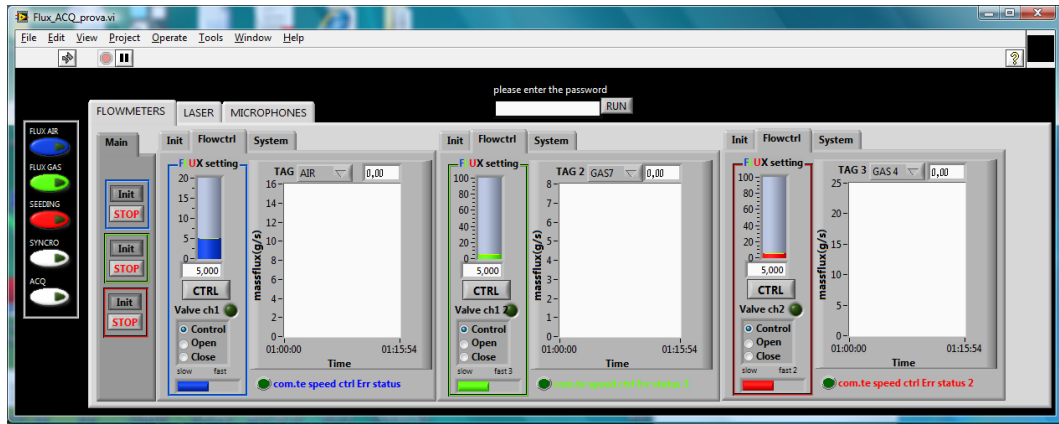
The hardware employed to investigate the aeroacoustic behaviour of RPE consisted in a laser, a CCD camera, a synchronizer, a loudspeaker, an ACQ board, a flowmeter and five microphones. All item were managed by means of the same software named SYNCHRO. SYNCHRO has been designed with three panels: flow-meters, laser and microphones.

Using the first panel is possible to send an instruction from a PC USB port to one of the available flow-meters (see Fig. A.6(a)). This signal is converted in a signal suitable for RS-485 protocol by a *black box* device. In this way very large RS-485 networks can be formed. Digital communications networks, implemented in RS-485 standard, can be actually used over long distances and in electrically noisy environments. Multiple receivers can be connected to such a network in a linear or multi-drop configuration, making it useful in industrial environments and similar applications. For the present experimental setup the linear network has been adopted and a scheme of wiring is reported in Fig. A.7.

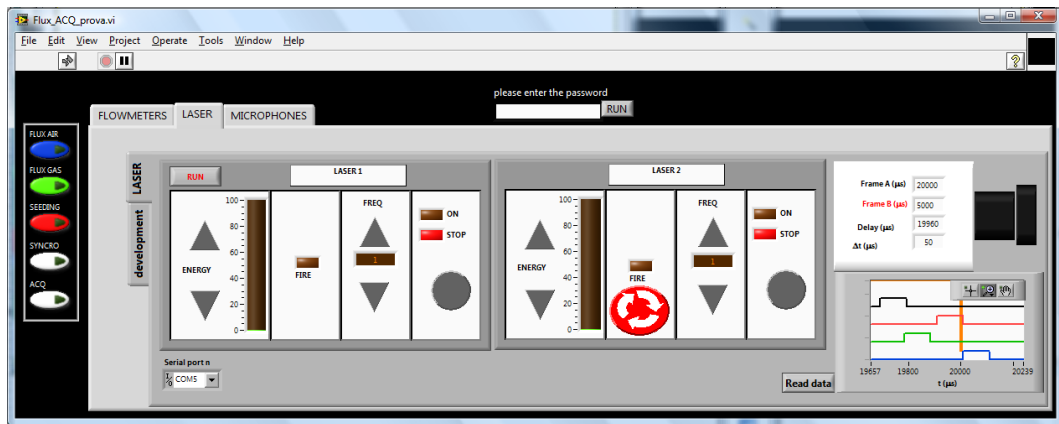
In Fig. A.6(b) the panel which controls the time delay between subsequent openings of the laser Q-switch is rendered. At the same time the opening of the CCD diaphragm is controlled sending a trigger signal to the camera. Finally the GUI of the software that acquires simultaneously the signal associated to the five microphones installed is shown in Fig. A.6(c).

A.4.2 easyPOD

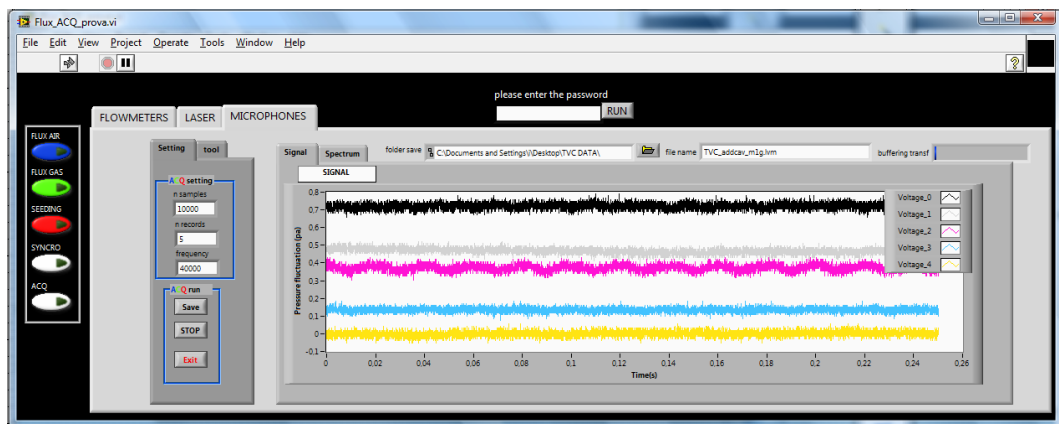
easyPOD is a home-made software devoted to the computation of the proper orthogonal decomposition of two dimensional fields. The GUI of the software



(a)



(b)



(c)

Figure A.6: GUI of the Flowmeter (a), Laser (b) and Microphones (c).

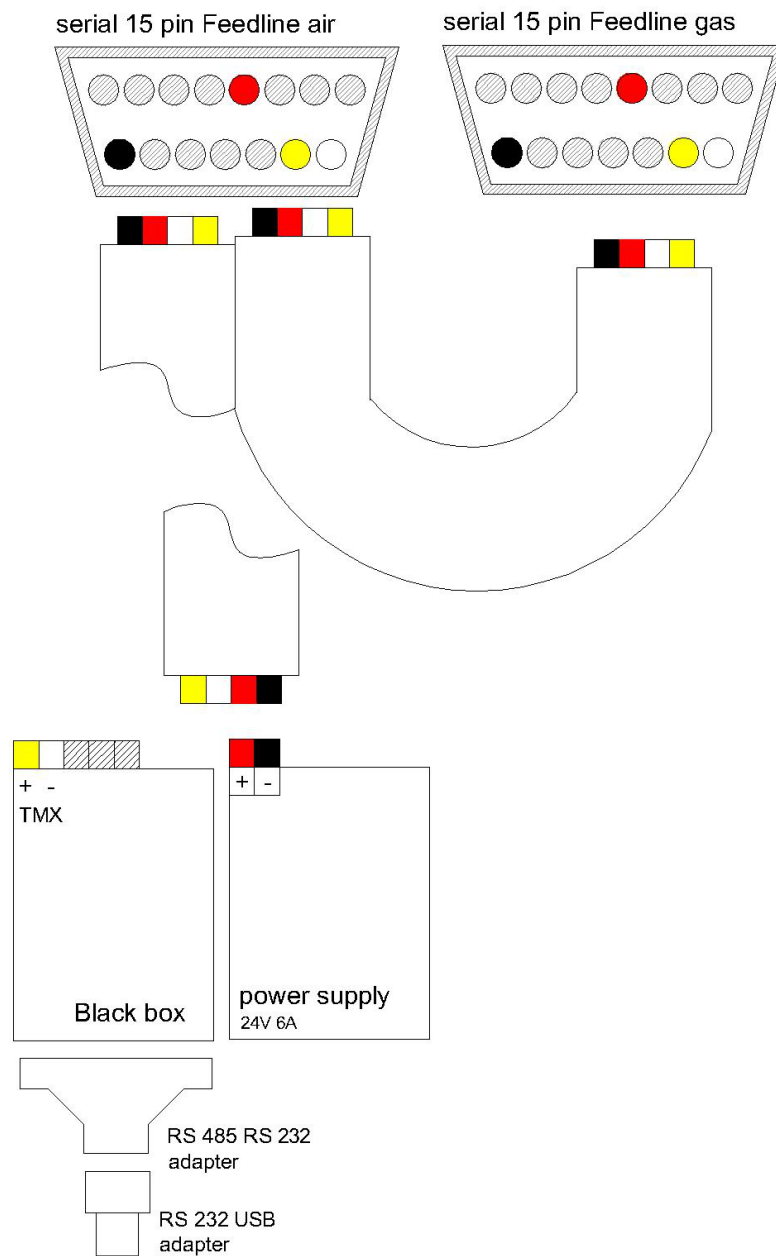


Figure A.7: Scheme of wiring of two different flow meter in a linear network.



Figure A.8: Icon of easyPOD.

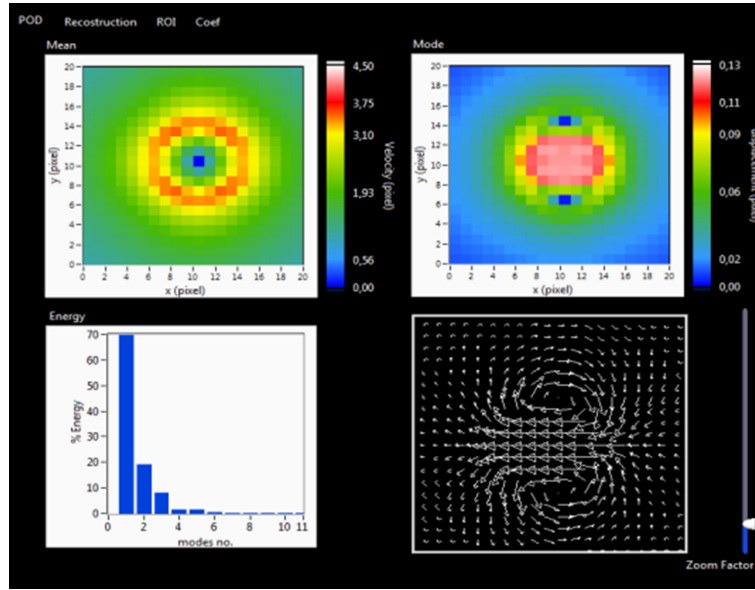


Figure A.9: GUI of easyPOD.

(see Fig. A.9) displays four graphes: the mean field (contour plot on the top-left side), the i -th mode (contour plot on the top-right side), the eigenvalues spectrum (on the bottom-left side) and the i -th mode on a quiver graph (on the bottom-right side).

The algorithm implemented in the main routine of easyPOD is resumed as follows:

1. reshaping of all velocity field in a vector \mathbf{u}^n , where $n \in [1, N]$ and N is the number of snapshots;
2. recasting the velocity field vectors in a matrix \tilde{U} :

$$\tilde{U} = (\mathbf{u}^1 \quad \dots \quad \mathbf{u}^N)$$

3. computing the cross-variance matrix $\tilde{C} = \tilde{U} \cdot \tilde{U}^T$;
4. solving the eigenvalue problem associated to \tilde{C} , $\det(\tilde{C} - \lambda_j \tilde{I}) = 0$
5. calculating the eigenvectors, \mathbf{A}_j , associated to \tilde{C} ;
6. finally computing the modes: $\Phi_j = \frac{\sum_{n=1}^N A_j^n \mathbf{u}^n}{\|\sum_{n=1}^N A_j^n \mathbf{u}^n\|}$

Bibliography

- R. J. Adrian. Statistical properties of particle image velocimetry measurements in turbulent flow anemometry in fluid mechanics. *Appl. Opt.*, 23: 115–129, 1984.
- K. K. Agarwal and R. V. Ravikrishna. Flow-acoustic characterisation of a cavity-based combustor configuration. *Defence Science Journal*, 61:523–528, 2011.
- H. M. Altay, D. E. Hudgins, R. L. Speth, and A. F. Ghoniem. Flame-vortex interaction driven combustion dynamics in a backward-facing step combustor. *Combust. Flame*, 156:1111–1125, 2009.
- H. M. Altay, D. E. Hudgins, R. L. Speth, and A. F. Ghoniem. Mitigation of thermoacoustic instability utilizing steady air injection near the flame anchoring zone. *Combust. Flame*, 157:686–700, 2010.
- G. K. Batchelor. *The theory of homogeneous turbulence*. Cambridge University Press, London, 1993.
- G. Berkooz, P. Holmes, and J.L. Lumley. The proper orthogonal decomposition in the analysis of turbulent flows. *annu. Rev. Fluid Mech.*, 250: 539–575, 1993.
- P. Bradshaw. Inactive motion and pressure fluctuations in turbulent boundary layers. *J. Fluid Mech.*, 30:241–258, 1967.
- T. F. Brooks and T. H. Hodgson. Tailing edge noise prediction from measured surface pressures. *J. Sound Vib.*, 1:67–117, 1981.

- J. C. Bruggeman, A. Hirschber, M. E. H. Van Dongen, and A. P. J. Winands. Self-sustained aero-acoustic pulsations in gas transport systems: experimental study of the influence of closed side branches. *J. Sound Vib.*, 150:371–393, 1991.
- C. Bruno and M. Losurdo. The trapped vortex combustor: an advanced combustion technology for aerospace and gas turbine applications. *Ad. Comb. and Aerothermal Technologies*, pages 365–384, 2007.
- R. Camussi, G. Guj, A. Di Marco, and A. Ragni. Propagation of wall pressure perturbation in a large aspect ratio shallow cavity. *Exp. Fluids*, 40:612–620, 2006.
- R. Camussi, M. Felli, F. Pereira, G. Aloisio, and A. Di Marco. Statistical properties of wall pressure fluctuations over a forward-facing step. *Phys. Fluids*, 20:075113, 2008.
- R. C. Chanaud. Effects of geometry on the resonance frequency of Helmholtz resonators. *J. Sound Vib.*, 178:337–348, 1994.
- G. M. Corcos. The structure of the turbulent pressure field in the boundary-layer flows. *J. Fluid Mech.*, 18:353–378, 1964.
- S. Grizzi and R. Camussi. Wavelet analysis of near-field pressure fluctuations generated by a subsonic jet. *J. Fluid Mech.*, 68:93–124, 2012.
- R. C. Hendricks, D. T. Shouse, W. M. Roquemore, D. L. Burrus, B. S. Duncan, R. C. Ryder, A. Brankovic, N.-S. Liu, J. R. Gallagher, J. A. Hendricksand, and J. A. Hendricks. Experimental and computational study of trapped vortex combustor sector rig with high-speed diffuser flow. *Int j. of Rotating Machinery*, 7:375–385, 2001.
- K. Y. Hsu, C. D. Carter, V. R. Katta, and W. M. Roquemore. Characteristics of combustion instability associated with trapped vortex burner. *19th AIAA Aerospace Science Meeting and Exhibit, Reno, NV*, 99-0488: 1–9, 1999.

- D. D. Trump K. Y. Hsu, I. P. Goss and W. M. Roquemore. Performance of a trapped vortex combustor. *Aerospace Science Meeting and Exhibit*, 33: 1–15, 1995.
- V.R. Katta and W. M. Roquemore. Numerical studies on trapped-vortex concepts for stable combustion. *J. for Engineering for Gas Turbine and Power*, 120:60–68, 1998.
- R. D. Keane and R. J. Adrian. Statistical properties of particle image velocimetry measurements in turbulent flow laser anemometry in fluid mechanics. *Meas. Sci. Technol.*, 1:1202–1222, 1990.
- R. D. Keane and R. J. Adrian. *Meas. Sci. Technol.*, 2:963–983, 1991.
- J. J. Keller. Nonlinear self-excited acoustic oscillations within fixed boundaries. *J. Fluid Mech.*, 123:267–281, 1982.
- J. J. Keller. Non linear self-excited acoustic oscillations in cavities. *J. Sound Vib.*, 94:397–409, 1984.
- J. J. Keller and M. P. Escudier. Flow-excited resonances in covered cavities. *J. Sound Vib.*, 86:199–226, 1983.
- H. Lamb. *Hydrodynamics*. Dover, London, 6th ed. edition, 1932.
- S. Maurel, J. Borée, and J.L. Lumley. Extended proper orthogonal decomposition: application to jet/vortex interaction. *Flow, Turb. and Comb.*, 67:125–136, 2001.
- K. E. Meyer, J. M. Pedersen, and Oktay’ozcan. A turbulent jet in crossflow analysed with proper orthogonal decomposition. *J. Fluid Mech.*, 583:199–227, 2007.
- N. Murray, E. Sällström, and L. Ukeiley. Properties of subsonic open cavity flow fields. *Phys. Fluids*, 21:353–364, 2009.
- Y. Na and P. Moin. The structure of wall-pressure fluctuations in turbulent boundary layers with adverse pressure gradient and separation. *J. Fluid Mech.*, 377:347–373, 1998.

- A. K. Nielsen. Acoustical resonators of circular cross-section and with axial symmetry. *Phil. Trans. Danish Ac. of Tec. Science*, 10:9–70, 1949.
- N. Noiray, D. Durox, T. Schuller, T., and S. Candel. A unified framework for nonlinear combustion instability analysis based on the flame describing function. *J. Fluid Mech.*, 615:139–167, 2008.
- A. D. Pierce. *Acoustics*. Acoustical Society of America, 1994.
- T. Poinso and D. Veynante. *Theoretical and Numerical Combustion*. Edwards, 2005.
- M. Raffel, C. Willert, and J. Kompenhans. *Particle image velocimetry*. 1998.
- A. Selamet, P. M. Radavich, N. S. Dickey, and J. M. Novak. Theoretical, computational and experimental investigation of Helmholtz resonators with fixed lumped versus distributed analysis. *J. Sound Vib.*, 187:358–367, 1995.
- A. Selamet, P. M. Radavich, N. S. Dickey, and J. M. Novak. Circular concentric Helmholtz resonator. *J. Acoustic. Soc. Am.*, 101:41–51, 1997.
- A. Singhal and R. V. Ravikrishna. Single cavity trapped vortex combustor dynamics - part-1: Experiments. *International journal of spray and combustion dynamics*, 3:23–44, 2011a.
- A. Singhal and R. V. Ravikrishna. Single cavity trapped vortex combustor dynamics - part-2: Simulations. *International journal of spray and combustion dynamics*, 3:45–62, 2011b.
- L. Sirovich. Turbulence and the dynamics of coherent structures. part 1: coherent structures. *Quart. App. Math.*, 3:561–571, 1987.
- M. Stanislas, K. Okamoto, C. J. Kähler, J. Westerweel, and F. Scarano. Main results of the third international piv challenge. *Exp. Fluids*, 45:27–71, 2008.
- G.J. Sturgess and K. Y. Hsu. Combustion characteristics of a trapped vortex combustor. *Gas Turbine Engine Combustion, Emissions and Alternative Fuels, Lisbon (Portugal)*, 1998.

- C. K. W. Tam. The acoustic modes of two-dimensional rectangular cavity. *J. Sound Vib.*, 49:353–364, 1976.
- C. K. W. Tam and P. J. W. Block. On the tones and pressure oscillations induced by flow over rectangular cavities. *J. Fluid Mech.*, 89:373–399, 1978.
- P. K. Tang and W. A. Sirignano. Theory of generalized Helmholtz resonator. *J. Sound Vib.*, 26(2):247–262, 1973.
- B. Venkatesham, M. Tiwari, and M. L. Munjal. Transmission loss analysis of rectangular expansion chamber with arbitrary location of inlet/outlet by means of green’s functions. *J. Sound Vib.*, 323:1032–1044, 2009.
- C. J. Wu, X. J. Wang, and H. B. Tang. Tansmission loss prediction on a single-inlet/double outlet cylindrical expansion-chamber muffler by using the modal meshing approach. *Applied Acoustics*, 69:173–178, 2008.
- F. Xing, S. Zhang, P. Wang, and W. Fanb. Experimental investigation of a single trapped-vortex combustor with a slight temperature raise. *Aerospace Science and Technology*, 14:520–525, 2010.
- F. Xing, P. Wang, S. Zhang, Y. Zhenga J. Zoua, R. Zhang, and W. Fanc. Experiment and simulation study on lean blow-out of trapped vortex combustor with various aspect ratios. *Aerospace Science and Technology*, 18: 48–55, 2012.
- S. Ziada. Flow-excited acoustic resonance in industry. *J. Pressure Vessel Technology*, 132:1–9, 2010.